crystals

MDPI

Review

On Directional Dendritic Growth and Primary Spacing—A Review

Joel Strickland, Bogdan Nenchev and Hongbiao Dong *

School of Engineering, University of Leicester, Leicester LE1 7RH, UK; jcjs2@leicester.ac.uk (J.S.); bn55@leicester.ac.uk (B.N.)

* Correspondence: h.dong@leicester.ac.uk; Tel.: +44-(0)-116-252-2528

Received: 8 June 2020; Accepted: 14 July 2020; Published: 20 July 2020

Abstract: The primary spacing is intrinsically linked with the mechanical behavior of directionally solidified materials. Because of this relationship, a significant amount of solidification work is reported in the literature, which relates the primary spacing to the process variables. This review provides a comprehensive chronological narrative on the development of the directional dendritic growth problem over the past 85 years. A key focus within this review is detailing the relationship between key solidification parameters, the operating point of the dendrite tip, and the primary spacing. This review critiques the current state of directional dendritic growth and primary spacing modelling, briefly discusses dendritic growth computational and experimental research, and suggests areas for future investigation.

Keywords: directional solidification; microstructure; dendritic growth; primary spacing; modelling

1. Introduction

Dendrite is a descriptive word derived from the Greek, "dendron", which means tree. In metallurgy, dendrites are arborescent crystalline structures that grow by diffusion-limited heat and mass transfer. At their origin, is undercooling below the freezing point of the solid and nucleation of a crystal. The accumulation of solute ahead of a growing interface can cause constitutionally undercooled zones [1,2], which under appropriate circumstances can become unstable and the solidification morphology dendritic. In metals, the surface energy is typically anisotropic and certain growth directions are energetically favoured. In most cubic metals, the preferential growth directions are <100>, which results in crystal growth parallel and opposite to the heat flow. As a result, metallic cubic dendrites exhibit crystallographically-related features, such as primary trunks, secondary and tertiary side arms, and sometimes arms of even higher order.

In directional solidification, the heat transfer is constrained through the solid, which results in primary trunk growth aligned opposite to the direction of heat flow. In the regime where the solid-liquid interface is strongly morphologically unstable, arrays of dendrites evolve from homogenous starting compositions, into complex spatio-temporal patterns far from equilibrium [3]. In the literature, single crystal patterns are classified as either square, hexagonal, or random [4]. The variation in composition between the advancing dendrite and the surrounding interdendritic region gives rise to microsegregation within the solidified crystal [5,6]. Normal to the dendrite growth direction, this segregation is characterised by the primary spacing, λ_1. The primary spacing controls the maximum length scale for the microsegregation [7], the solutioning heat treatment times [8,9], and the mechanical properties of the directionally solidified material [10–24]. In addition, the λ_1 directly influences the mushy zone convection, the formation of low melting point secondary phase eutectics, as well as incoherent precipitates and pores in the interdendritic region [25–32]. Consequently, the mechanical

properties of unidirectional solidified crystals are strongly dependent on the temperature and convection within the melt, as this controls the concentration of solute at the solid–liquid interface.

In the literature, a significant amount of steady state solidification work is reported that characterises the relationship between primary spacing, alloy composition, C_0, thermal gradient, G, and tip growth velocity, V [33–41]. In directional solidification, the G and V can be independently controlled, so one may study the dependence of λ_1, on either G (at constant V) or V (at constant G). Over the years, the fundamental understanding of the relationship between dendrite tip growth and primary spacing has improved considerably. Theoretical models and extensive experimental studies have now established criterion to determine dendrite tip radius as a function of the growth parameters [42–44]. During the same period, primary spacing modelling has undergone its own arduous empirical and theoretical journey, whereby researchers have concentrated on relating the tip growth kinetics to the resultant microstructural patterns [40,41,45–50]. As a result, the primary spacing was linked to the process variables by the following non-linear steady state relationship:

$$\lambda_1 = AC_0^{0.25}V^{-0.25}G^{-0.5}. \quad (1)$$

Current day solidification science has developed into a massive international community. The field has diverged into a variety of casting, characterisation, modelling, and defect prediction-specific areas; for a broader overview, the reader is directed to references [51,52]. Directional dendritic growth and primary spacing modelling still piques the interest of a significant number of researchers, with many tantalising challenges and tangible rewards for society still available. For this reason, the aim of this review is to provide a comprehensive chronological narrative on the development of the directional dendritic growth problem over the last 85 years. The authors elucidate the relationships between key processing parameters, the operating point of the dendrite tip, and the primary spacing. This review critiques the current state of primary spacing modelling, briefly discusses dendritic growth computational and experimental research, and concludes by suggesting directions for future research.

2. The Operating Point of a Dendrite Tip (1935–1999)

Modelling of directionally solidified microstructural patterns, first requires a theoretical understanding of the growth of an isolated dendritic tip and determination of a steady state solid–liquid interface shape (Figure 1). In 1935, Papapetrou [53] proposed that a parabolic interface satisfied the shape preserving condition. The author reasoned that if only part of the latent heat was rejected ahead of the growing dendrite, a fixed concentration profile and shape would be maintained.

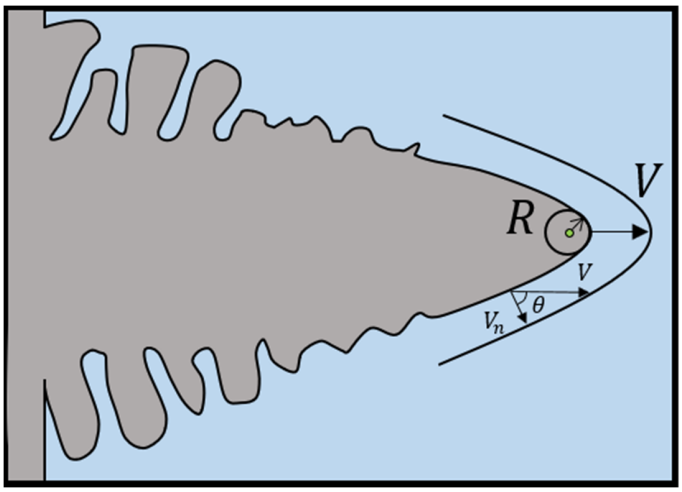

Figure 1. Shape preserving condition for steady state growth of a dendrite tip. V is the dendrite tip growth velocity; R is the dendrite tip radius; V_n is the normal velocity required to maintain the steady state shape.

In 1947, Ivantsov [42] provided elementary mathematical treatments for an isothermal parabolic plate-like dendrite (2D) and a paraboloid of revolution (3D needle crystal) with an isoconcentrate interface. Ivantsov solved the self-consistent shape preserving condition for steady state dendritic tip growth with the following equations:

for the 2D case,

$$\Omega_C = \sqrt{\pi P_c}\, exp^{P_c}\left(1 - erf\sqrt{P_c}\right), \tag{2}$$

and the 3D case,

$$\Omega_C = P_c exp^{P_c} E_1(P_c), \tag{3}$$

where, P_c is the solute Péclet number ($VR/2D$); V is the dendrite tip growth velocity; R is the dendrite tip radius; D is the liquid solute diffusivity; $E_1(P_c)$ is the exponential integral; Ω_C is the dimensionless solute undercooling $(C_t - C_0/C_t(1-k))$; C_t is the composition in the liquid at the dendrite tip; C_0 is equilibrium alloy composition; k is the solute partition coefficient. Later, the Ivantsov analysis was extended by Horvay and Cahn [54] to paraboloids with elliptical cross-sections. These researchers generalised the Ivantsov solutions for a paraboloid of revolution by expressing the dendritic surface in dimensionless variables and varying the eccentricity of the elliptical cross-section. In the isotropic case, these quasi-stationary Ivantsov solutions describe the dendritic tip shape as a smooth sphere. However, in the anisotropic case, the sphere is deformed in the direction of the anisotropy strength. For a given tip undercooling, ΔT, the Ivantsov solutions produced an infinite set of V and R combinations that satisfied the requirement of $V \times R = constant$ (Figure 2). Therefore, for a given set of growth conditions, no unique solution was determined for the dendritic tip operating point. Thus, an additional selection constraint independent of energy transport was required.

Around the same time as Ivantsov was publishing his seminal work, Zener [55] was introducing the concepts of diffusion and capillarity in the form of equations for the lengthening of needle crystals in lamellar phase transformations. Although Zener was investigating solid-state transformations, the associated physical phenomena were in many ways like that which occurs in dendritic growth. Zener realised that the inclusion of capillarity produced a maximum in the $V - R$ curve and suggested a phase change occurred at the greatest growth rate ('Extremum Condition'), rather than at the lowest free energy. Hillert [56] found Zener's diffusion-controlled model to be inaccurate for high supersaturations and modified it by deriving an approximate analytical solution for the diffusion equation that related time and structure. The Zener–Hillert model established the theoretical foundation for diffusion-controlled growth kinetics of lamellar phases and explained the relationship between lamellar spacing, ΔT, and V during the phase transition.

2.1. The Extremum Condition

In the 1960's, Temkin [43] and Bolling and Tiller [57] pointed out the nonisothermal nature of the interface due to interface curvature and interface kinetics, which made the actual steady-state dendritic tip shape deviate from a paraboloid of revolution. The researchers subsequently included the stabilising effect of the interface energy and/or interface attachment kinetics in an attempt to provide a unique solution to the Ivantsov equations. However, the addition of capillarity did not remove the multiplicity of predicted V and R combinations; unfortunately, only the very small dendrite tip radii solutions were unstable (Temkin Curve—Figure 2). To overcome this problem and provide an exact solution to the Ivantsov equations i.e., determine the operating point of a steadily growing dendrite tip, many authors [43,57–61] applied the 'extremum condition' as suggested by Zener.

In 1965, Jackson and Hunt discovered low melting point organic transparent materials that froze like metals, and performed the first in-situ observations of dendritic pattern formation [62,63]. Following their pioneering work, Glicksman et al. [64,65] demonstrated that succinonitrile could realistically simulate metal solidification and investigated the current steady state dendritic tip growth theories. Their experiments confirmed that application of the extremum condition predicted R over an order of magnitude larger than observed experimentally [64]; thus, a new tip selection theory

was required. Glickman's seminal work, was fundamental in validating the theory of constitutional undercooling suggested by Ivantsov [1] and Tiller et al. [2] over a decade earlier.

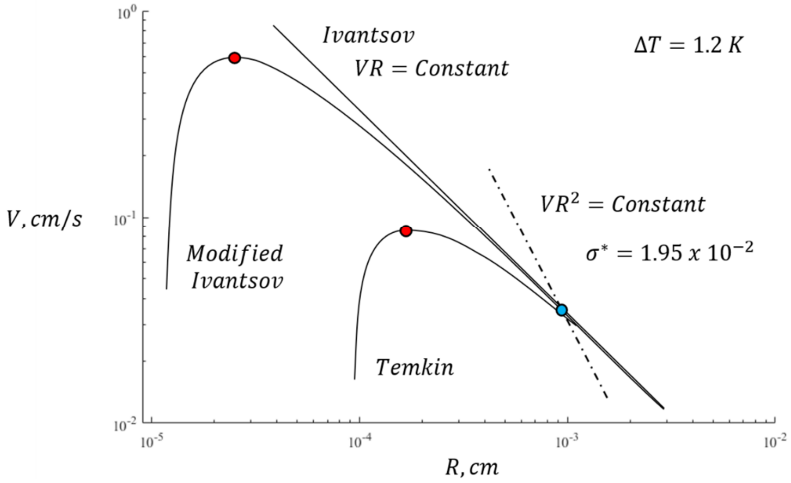

Figure 2. Dendrite tip growth rate, V, as a function of the tip radius, R, for constant undercooling, ΔT, in pure succinonitrile. Extremum condition indicated by the red circles on the Modified Ivantsov and Temkin curves. Marginally Stable point indicated by blue circle. Plot adapted from [66].

2.2. The Marginal Stability Condition

In 1973, Oldfield performed the first computer calculations of dendritic behaviour [67]. Oldfield's work was strictly numerical and suggested that the dendritic tip operated between a balance of the stabilising effect of capillarity and the destabilising effect of diffusion or thermal conduction. Under the assumption of steady state heat flow, Oldfield's stability criterion is expressed as:

$$\sigma^* = \frac{2\alpha d_0}{VR^2} = 0.02, \tag{4}$$

where, σ^* is the stability criterion; α is the thermal diffusivity; d_0 is the capillary length $\left(T_m\gamma C_p/L^2\right)$; T_m is the melting point; γ is the surface tension of the solid–liquid interface; C_p is the heat capacity of the liquid phase; L is the heat of fusion. It is worth noting that the Ivantsov thermal diffusion models (Equations (2) and (3)) were derived using an isothermal interface, $\gamma = 0$.

In 1978, Langer and Müller-Krumbhaar (LM–K) [68,69] applied a Mullins and Sekerka [70,71] type stability analysis to calculate the additional physical principle required to find the operating state of a steadily growing dendrite tip. According to Mullins and Sekerka, for a crystal with a planar solid/liquid interface to grow stably, the wavelength of perturbation at the interface must be smaller than:

$$\lambda_s = 2\pi\sqrt{2\alpha d_0/V}, \tag{5}$$

where, λ_s is the critical perturbation wavelength. LM–K suggested that dendritic tips grew at the 'marginally stable' operating point, rather than at maximum growth velocity (Extremum Condition—Figure 2). They took an Ivantsov parabola-type dendrite growing in a pure undercooled melt and considered a small departure from the parabolic tip shape caused by the interfacial energy effect [72], illustrated in Figure 3a. LM–K assumed a steady state planar interface exists at the dendrite tip and that the tip shape changes only slightly when isotropic capillarity is introduced. The criterion from equation (4) became:

$$\sigma^* = \frac{2\alpha d_0}{VR^2} = \frac{1}{4\pi^2} = 0.0253. \tag{6}$$

LM–K concluded that any tip radii smaller than the extremum point (Figure 2) would be unstable due to the increasing influence of capillarity. Their qualitative suggestion was that the dendrite tip

becomes as large as possible before becoming so large that tip-splitting occurs; it operates at the marginally stable point (Figure 2). However, the marginally stable point only confirmed that diffusion and capillarity were important characteristics of the physics behind dendrite formation. It did not provide any information regarding why a dendrite chooses the marginal stable state over other stable states [72].

In 1981, Huang and Glicksman (H–G) performed a test of Equation (6) and measured the dendrite tip V and R experimentally [66]. The researchers determined $\sigma^* = 0.0195$, which was within the computational uncertainty of the LM–K steady state planar tip interface model and near the lower uncertainty limit of the theory. The σ^* predicted by Equation (6) agreed within 25% of H–G's experimentally determined values. To account for proper local curvature at the dendrite tip, H–G approximated the tip interface as a sphere (Figure 3b). They noted the wavelength of perturbation around a sphere of radius R is a function of the spherical harmonic, n. To be consistent with the LM–K assumption that dendritic tip radius approximates to λ_s, H–G selected $n = 6$. The stability criterion in Equation (6) now reduced to:

$$\sigma^* = \frac{2\alpha d_0}{VR^2} = 0.0192. \tag{7}$$

H–G's modified spherical tip model agreed within 1.5% of their experimental results. They demonstrated that when the influence of container walls and other environmental factors were eliminated, σ^* obtained an excellent fit with experimentally determined stability criteria.

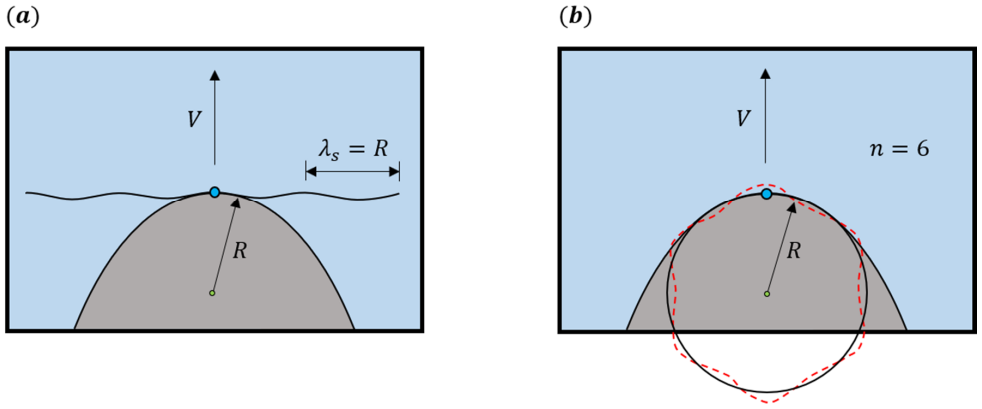

Figure 3. Schematics showing models for estimating dendrite tip stability: (**a**) perturbation of a planar interface at the marginally stable condition; (**b**) spherical interface model at a marginal stability condition with harmonics $n = 6$. Schematics adapted from [66].

2.3. The Microscopic Solvability Condition

In the 1980's, several authors [39,44,73–79] solved the self-consistent dendrite growth problem. Their equations balanced the thermal and solutal fields with the capillarity effect whilst satisfying the shape preserving condition. These researchers demonstrated that when either surface tension or surface kinetics are included, the continuous family of parabolic Ivantsov-like solutions are destroyed/eliminated. This is because the solid–liquid interface energy for crystalline materials is anisotropic, therefore, only when it was included did one of the solutions remain stable with respect to tip-splitting modes [80]. For small values of γ the solvability condition was demonstrated to be proportional to:

$$\sigma^* = \frac{2\alpha d_0}{VR^2} \cong \sigma_0 \varepsilon^{1.75}, \tag{8}$$

where, σ_0 is a numerical constant on the order of unity, defined with help of asymptotic methods; ε is a measure of fourfold anisotropy of the interface energy ($\gamma \propto [1 - \delta\cos(4\theta)]$); δ is the strength of anisotropy; θ is the angle between dendrite surface normal and its axis [51]. This new theoretical approach was designated the "microscopic solvability criterion" and provided a much firmer

fundamental basis than marginal stability (Equation (7)). The name reflected the interplay of microscopic d_0, which imposes a solvability condition on a family of macroscopic steady state tip solutions [81]. The theory demonstrated that marginal stability was still the main selection parameter, but the value of σ^* depended on the crystalline surface-tension anisotropy of the material. Unfortunately, due to the difficulty in calculating anisotropy, the predicted microscopic solvability tip selection parameter was only approximate in three-dimensions. Since predictions assumed an axisymmetric dendritic tip shape, there was inconsistent agreement between theory and experimental values [81]. Although the marginal stability constant has no real physical basis, it is simple to implement and predicts the operating point of a dendrite with reasonable accuracy.

2.4. A Test of Theory

To examine and test the diffusion-limited dendritic growth theories, Glicksman et al. [82] proposed an isothermal dendritic growth experiment in microgravity. The purpose was to greatly reduce the influence of convective heat and mass transport on dendrite tip selection. The reduction in buoyancy-driven convection enabled Glicksman et al. to study dendrite growth via only gravitationally independent sources of heat and mass transfer. By using a low Péclet number transparent organic analogue, they were able to study 'convection free' growth and measured the true growth kinetics and morphology of dendrites. The results from various microgravity experiments [83–88] concluded that the dendrite tip can be approximated as a paraboloid of revolution, as suggested by Papapetrou [53] 60 years earlier. This fundamental work validated the pure diffusion part of the dendritic growth theory with a tip selection rule of the form of Equation (8).

3. Primary Spacing Selection in Directional Solidification (1979–2004)

Directionally solidified microstructures are formed of complex spatio-temporal patterns, which when viewed normal to the array growth direction, are characterised by the λ_1 (Figure 4). The range of λ_1 within a solidified component determines the distribution of inhomogeneities in the material, which significantly influences the final mechanical properties [51,52]. The λ_1 varies with alloy composition, C_0, and solidification process variables, such as, thermal gradient, G, growth velocity, V, and melt flow. In constrained growth, the system variables can be independently controlled, so one may study the dependence of λ_1, on either G (at constant V) or V (at constant G).

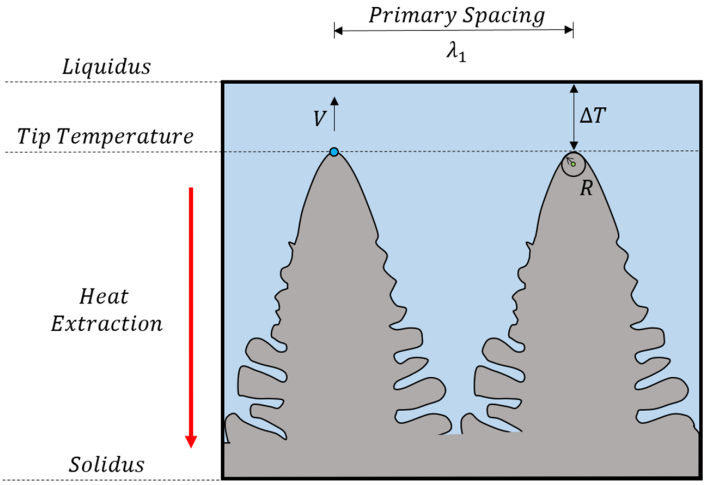

Figure 4. In directional solidification, most metallic cubic dendrites grow in arrays parallel and opposite to the heat flow direction. The primary spacing, λ_1, characterises twice the maximum diffusion distance between advancing neighbouring dendrites. Solute interaction between dendrites occurs within the interdendritic region and this influences the segregation pattern within a directionally solidified material. The blue dot indicates the operating point of the dendrite tip.

3.1. Early Primary Spacing Models

In 1979, Hunt developed the first model that linked directional solidification process variables with λ_1 [45]. The author approximated the arborescent dendritic shape as a smooth steady-state interface and derived a self-consistent interface shape using an approach developed by Brower, Brody, and Flemings [89]. In Hunt's model, the temperature and liquid composition varied only in the growth direction. However, this assumption was not valid for the derived steady state interface near the tip. To overcome this problem, the author fitted part of a sphere at the tip and obtained a relationship between R and λ_1. Following this, Hunt derived a relationship between R and ΔT for a spherical tip shape using a method similar to that described by Burden and Hunt [90]. As a result, Hunt was able to obtain a relationship between ΔT and λ_1. By assuming the dendrite tip advanced at the minimum undercooling (extremum condition—Figure 2), Hunt obtained a relationship between λ_1 and the process variables for the low and high V regimes as follows:

low V regime,

$$\lambda_1 = 2.83\left(\Delta T_0 D\Gamma k - \frac{kGD}{V}\right)^{0.25} V^{-0.25} G^{-0.5}, \tag{9}$$

high V regime,

$$\lambda_1 = 2.83(\Delta T_0 D\Gamma k)^{0.25} V^{-0.25} G^{-0.5}, \tag{10}$$

where, Γ is the Gibbs–Thomson coefficient; ΔT_0 is the equilibrium solidification range $(-m(1-k)C_0/k)$; m is the slope of the liquidus.

In 1981, Kurz and Fisher (K–F) [46] proposed a new general framework for relating R, ΔT, and λ_1 in alloy dendritic growth. The researchers used a simplified version of the Ivantsov solution (Equation (3)) to determine the solute-diffusion-limited growth of the dendrite tip i.e., the steady state interface shape. They applied the marginally stable tip operating point (Equation (7)) and developed a relationship between R and the process variables. The researchers approximated the dendritic interface shape as an ellipsoid and the local arrangement as hexagonal. In this way, the R could be related to the minor and major axes of the ellipsoid and to the λ_1 through geometric considerations. K–F calculated λ_1 for the low and high V regimes as follows:

low V regime,

$$\lambda_1 = \left[\frac{6\Delta T'}{G(1-k)}\left(\frac{D}{V} - \frac{\Delta T_0 k}{G}\right)\right]^{0.5}, \tag{11}$$

high V regime,

$$\lambda_1 = 4.3\Delta T'^{0.5}\left(\frac{D\Gamma}{\Delta T_0 k}\right)^{0.25} V^{-0.25} G^{-0.5}, \tag{12}$$

where, $\Delta T'$ is the difference between the non-equilibrium solidus and the tip temperature $(T_L - T_e - \Delta T)$; T_L is the liquidus temperature; T_e is the eutectic temperature. K–F compared their model to Trivedi's results [91] for isolated dendrite growth operating at marginal stability and found major differences occurring at high V due to the simplified approximation of the Ivantsov equation. However, even with major simplifications, they were able to match ΔT and R predicted by Trivedi's model with reasonable accuracy. The application of the marginal stability criterion within the K–F model avoided predicting dendrite tip radii too small, a problem usually associated with the extremum condition (Figure 2). K–F also predicted a new phenomenon, that the $\lambda_1 - V$ relationship was split into two regimes, one for cells at low V and one for dendrites at high V.

3.2. Precisely Controlled Experiments

In 1982, Mason et al. [92] performed some very careful constrained growth experiments on Pb–Sn alloys. These researchers explained how previous directional solidification experimental analysis was carried out over a limited range V, G, and C_0. Therefore, no consistent data existed which enabled accurate prediction of λ_1 as a function of these process variables [39]. They concluded that

the customary relationship found in the literature, $\lambda_1 = KG^{-a}V^{-b}$, implied the effects of C_0, G and V on λ_1 were independent of each other. However, their results suggested the effects of G and V were strongly coupled.

Following this, K. Somboonsuk et al. [93] performed further constrained growth experiments, this time using the most completely characterised material used in dendritic growth experiments, succinonitrile (SCN). The purpose was to carefully characterise the relationship between R and λ_1 as functions of V and temperature in the liquid. Their results concluded that when the solid–liquid interface is an isoconcentrate, the dendrite tip maintains a parabolic shape. Three important conclusions from their work were reached: (1) experimentally obtained R must match those predicted by an isolated dendrite model; (2) a sharp decrease in λ_1 occurs at the dendrite-to-cell transition V, which corresponds to a minimum in solute Péclet number; (3) in the high V regime, a variation in G significantly alters the λ_1 but has no effect on R or secondary dendrite spacing, λ_2; their experimental results are illustrated in Figure 5.

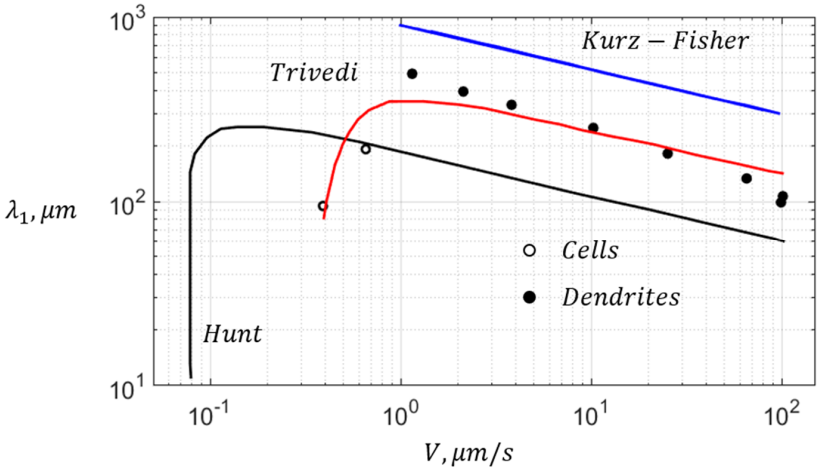

Figure 5. Comparison between Hunt [45], Kurz–Fisher [46] and Trivedi [47] primary spacing, λ_1, models using experimental data from Somboonsuk et al. [93]. Plot adapted from [47].

3.3. An Improved Analytical Primary Spacing Model

In 1984, Trivedi [47] compared the models of Hunt and Kurz–Fisher with experimental data of K. Somboonsuk et al., [93] (Figure 5). At high V, both models demonstrated the same functional relationship of the variables V and G, and the Kurz–Fisher model predicted the dendrite-to-cell transition accurately. However, the experimental line had a higher gradient than that predicted by either theory. Furthermore, the Kurz–Fisher model predicted a primary spacing 1.3–2 times too high and the Hunt model 1.8–3 times too small. In addition, the relationship $V^{-\frac{1}{4}}G^{-\frac{1}{2}}$ was shown to not characterise the λ_1 in the low V regime where cells are formed, hence, a more complicated equation in the form of $V^{-x}G^{-y}$ was required.

To provide a better description of the experimental results of Somboonsuk et al. [93], Trivedi [47] modified the λ_1 and R relationship derived by Hunt [45] with the marginal stability criterion (Equation (7)). Following this, Trivedi determined R using a quadratic equation developed earlier for isolated dendritic growth [91] that related P_c to V, G and C_0. For a given value of P_c the author obtained two stable combinations of V and R, whereby one set corresponded to the dendritic region and the other to the cellular. Trivedi's steady state primary spacing model is as follows:

$$\lambda_1 = 2.83(\Delta T_0 k D \Gamma L)^{0.25} V^{-0.25} G^{-0.5}, \tag{13}$$

where, $L = \frac{l}{2}(l+1)(l+2)$ for the spherical approximation of the dendrite front (Figure 3b); l is the harmonic of perturbation which equals six for the dendrite growth process [66,93]. Trivedi's model

demonstrated good agreement with the results of K. Somboonsuk et al. [93] (Figure 5). The model predicted the maximum λ_1 as a function of V with good accuracy. Furthermore, it demonstrated that the dendrite-to-cell transition occurred when the thermal gradient effect became significant i.e., when the Péclet number increased towards infinity, which was accompanied by a reduction in λ_1. However, Trivedi's model deviated from experiment at high V and lacked a proper theoretical treatment of the cell-to-dendrite transition. Trivedi [47] summarised two important aspects for further theoretical attention: (1) a more accurate relationship between λ_1 and R was required to properly predict the slope of the log λ_1 versus log V; (2) a theoretical description of the dendrite and cell characteristics in the region where both of these morphologies exist.

3.4. The Stable Range of Primary Spacing

In the past, many authors concentrated on measuring average values of λ_1 for a fixed growth condition and comparing with a unique theoretical value [94,95]. However, a growing body of theoretical and experimental evidence regarding cellular spacings indicated that a wide range of stable spacings were possible for a given set of growth conditions [93,96–99]. In fact, wide distributions of λ_1 were regularly observed across transverse sections in metallic alloys [100,101].

In 1990, Warren and Langer (W–L) [102] proposed there existed a continuous range of physically allowable λ_1, therefore, removing the necessity for an additional λ_1 selection condition to distinguish one unique λ_1. They suggested the final λ_1 depended upon the sequence of events by which the system is set into motion. The researchers set up a periodic array of dendrites consistent with both microscopic solvability theory and the macroscopic equations for the solute diffusion field. W–L then applied a Mullins and Sekerka [70,71] type linear stability analysis to a planar solid–liquid interface and calculated the crossover wavelength for the onset of instability i.e., the lower λ_1 stability bound. Their model demonstrated a reasonable agreement with the experimental results of Somboonsuk et al. [93]. However, it was only applicable when weak local dendritic coupling occurred i.e., at moderate growth velocities. In 1993 [103], W–L modified their earlier model to follow the formation of a dendritic array from the initial instability of a planar solidification front to the selection of a final steady state array λ_1 (Figure 6). They examined the morphological stability of the leading edge and used nonlinear terms to describe the development of the dendritic array. Three sequential mechanisms were incorporated into their work: (1) buildup of a solutal boundary layer in front of an initial flat interface; (2) onset of morphological instability and formation of a relatively fine array of dendritic tips; (3) array coarsening. The modified model predicted the moderate V lower stability bound for the experimental results of Ding et al. [104] with excellent accuracy. However, it lacked a theoretical treatment of cellular formation or inclusion of the mechanisms behind tertiary arm branching (Figure 9b). Although it had many approximations and theoretical assumptions, their work determined some of the key aspects of non-linear interface stability analysis and predicted a new phenomenon; spatial period-doubling bifurcation (the W–L overgrowth condition).

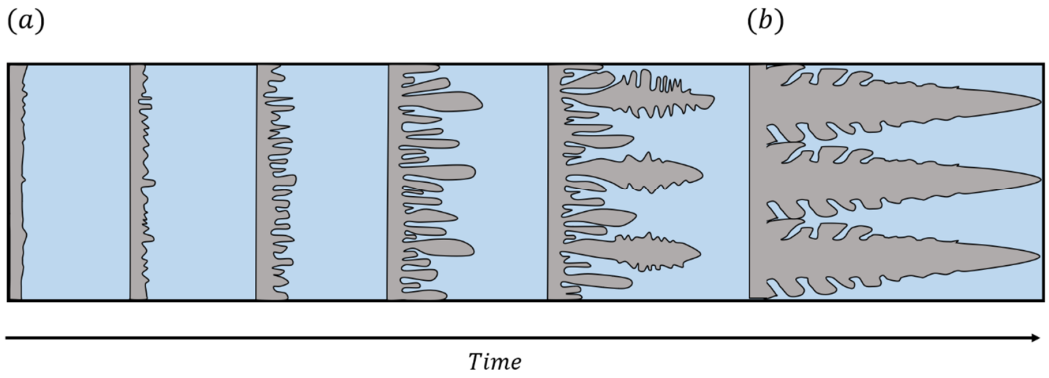

Figure 6. Schematic of the development of an (**a**) initial instability of critical size into a (**b**) final steady state dendritic pattern with uniform array λ_1. Schematic adapted from [103].

3.5. The First Numerical Primary Spacing Model

In 1992, based on earlier developmental work [105,106], Lu and Hunt (L–H) created the first truly numerical primary spacing model [107]. Originally the model was developed to study cellular arrays, however, it was extended to dendrites when it appeared to be making correct predictions. The model used a simple, fully implicit, control volume method [108,109] to solve the diffusion problem and maintain a self-consistent dendrite interface shape. By including a non-zero surface energy they found a singular solution to the dendritic growth problem; confirming the importance of anisotropy on selection of the tip radius as developed separately by the microscopic solvability approach (Equation (8)). L–H provided the first theoretical framework to calculate the lower primary spacing bound for a fixed set of growth conditions by considering transport of solute between multi-cell walls (Figure 7b) and determined the upper spacing bound by multiplying minimum array spacing by a factor of two (Figure 8). The idea was that a local λ_1 that is twice the lower stability limit would reduce solute interaction between neighbours sufficiently to allow a tertiary arm to catch up with the growth front (Figure 9b). No model beforehand [45–47] had been able to predict the distribution of λ_1 without making arbitrary assumptions about the selection procedure or without using an oversimplified solution to the diffusion problem [107]. Their model successfully predicted the onset of the constitutional and absolute stability limits, the formation of cells at low and very high V, and the cell–dendrite–cell transition velocities. Furthermore, the model predicted that a range of stable λ_1 existed for cells and dendrites around the transition velocity.

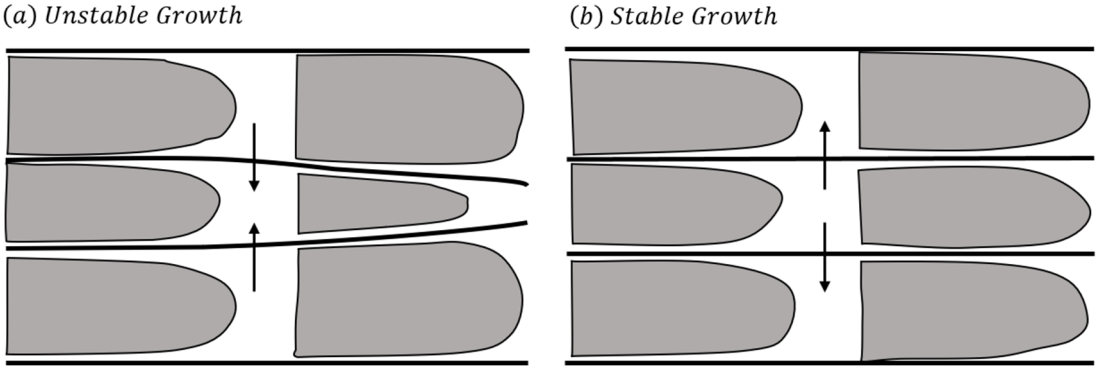

Figure 7. Schematic illustration of the direction of solute flow at the cell walls for (**a**) overgrowth and (**b**) array stability. Schematic adapted from [107].

In 1994, L–H extended their earlier numerical model [107] into the high V region by considering a variable k and non-constant liquidus slope [110]. Additionally, these researchers included a modified undercooling equation where k was adjusted for solute trapping at high V. The R and ΔT values from the numerical results were compared to the analytical KGT dendritic tip model for rapid solidification [111] and demonstrated a reasonable agreement. Following this, by suitable nondimensionisation, Hunt and Lu [49] gave analytic expressions to fit their numerical results [107,110].

For cellular growth,

$$\lambda_1{}' = 4.09k^{-0.485}V'^{-0.29}(V' - G')^{-0.3}\Delta T_s'^{-0.3}(1 - V')^{-1.4}, \tag{14}$$

for dendrite growth,

$$\lambda_1' = 0.7798 \times 10^{-1}V'^{(a-0.75)}(V' - G')^{0.75}G'^{-0.6028}, \tag{15}$$

where,

$$\lambda' = \frac{\lambda\Delta T_0}{\Gamma k}, \qquad G' = \frac{G\Gamma k}{(\Delta T_0)^2}, \qquad V' = \frac{V\Gamma k}{D\Delta T_0}, \qquad \Delta T_s' = \frac{G'}{V'} + V'^{0.333},$$

and

$$a = -1.131 - 0.1555\log_{10}(G') - 0.007589\left[\log_{10}(G')\right]^2.$$

In Equations (14) and (15), the dimensionless primary spacing, λ', refers to the radius rather than the diameter. Following this, Hunt and Thomas [112] modified Equation (15) for the case of alloy systems where $k \to 0$ as it was found that the reformulated expression behaved more realistically. According to Hunt [113], the minimum primary spacing or array stability limit is now given by the smaller of the following two equations:

$$\lambda_1' = 2.5{V'}^{-b}\left(1 - \frac{G'}{V'}\right)^{0.5} {G'}^{-\frac{2(1-b)}{3}}, \tag{16}$$

or,

$$\lambda_1' = 12{V'}^{-1}, \tag{17}$$

where,

$$b = 0.3 + 1.9{G'}^{0.18}.$$

The analytical results provided an insight into the directional dendritic growth processes–property relationships and enabled theory to be compared quickly with experimental results. The Hunt–Lu model can predict λ_1 under a range of growth conditions for a variety of alloys (Figure 8). However, as this model was originally developed to study cellular growth (Figure 7), it lacks the physical mechanism to determine the upper spacing limit by tertiary arm branching (Figure 9c).

3.6. Understanding the Primary Spacing Selection Process

Following the work of Warren and Langer [103] and Lu and Hunt [107], Huang et al. [114] set out to experimentally determine the lower and upper λ_1 stability limits for a wide range of G and V. To find the upper λ_1 bound for a fixed set of conditions, the researchers first formed a stable dendritic array (Figure 9b) and then step-increased the pulling velocity, V_p, until the array became unstable; ensuring enough time at each velocity step for array stability. For the lower λ_1 stability limit, Huang et al. applied the same method, however this time using a step-decreasing V_p. Their findings suggested that the lower and upper λ_1 stability limit for a fixed set of growth conditions are absolute, but the average array λ_1 is remarkably history-dependent. Furthermore, they found good agreement between their experimentally determined lower λ_1 stability limit and that predicted by the modified W–L model [103]. The history-dependent results of Ding et al., [104] are plotted in Figure 8 against the most sophisticated λ_1 models to illustrate current predictive capability.

In 1994, Han and Trivedi (H–T) [48] performed constrained dynamic growth experiments on a SCN-acetone system to understand the λ_1 selection process. The researchers confirmed the results of Huang et al. [114,116], that a range of stable array λ_1 can exist for a given set of experimental conditions. Below the lower stability limit the array is unstable and dendrite elimination occurs by overgrowth increasing the local spacing (Figure 9a). Above the upper stability limit, tip-splitting for cells or new dendrite formation by tertiary branching occurs decreasing the primary spacing (Figure 9c).

These researchers observed a new time-dependent array adjustment mechanism, which refined the Gaussian distribution of array λ_1 with time by slow lateral dendrite migration and defect interaction with the growth front (Figure 10). H–T suggested that due to the sluggish nature of this readjustment mechanism, it may not be possible to reach a steady state uniform spacing (Figure 6b) within the finite time of a given experiment. To understand the factors that may be important in determining stable λ_1 range for a given set of growth conditions, a simple global mass balance model was developed. They assumed some arbitrary interface shapes and developed a general relationship between λ_1 and the characteristics lengths:

$$\lambda_1 = \mathrm{A}[l_D]^{0.25}[l_T]^{0.5}[d_0]^{0.25}, \tag{18}$$

where,

$$A = \frac{\alpha}{\sqrt{k}}\left[\frac{1}{2\sigma^*}\right]^{0.25},\ l_D = \frac{2D}{V},\ l_T = \frac{mC_t(1-k)}{G},\ d_0 = \frac{\Gamma}{mC_t(1-k)},$$

where, A is a proportionality constant; l_D is the solutal length; l_T is the thermal length; d_0 is the capillary length. Equation (18) gave clear insight into the role of the experimental variables on λ_1 selection at low velocities. The equation indicates that a change in G only influences l_T, whereas a change in V alters only l_D, and that both d_0 and l_T are influenced by a change in composition as a result of a change in the solidification range. Furthermore, the theoretical analysis of H–T demonstrated that the primary spacing was proportional to the geometric mean of $R \times l_T$.

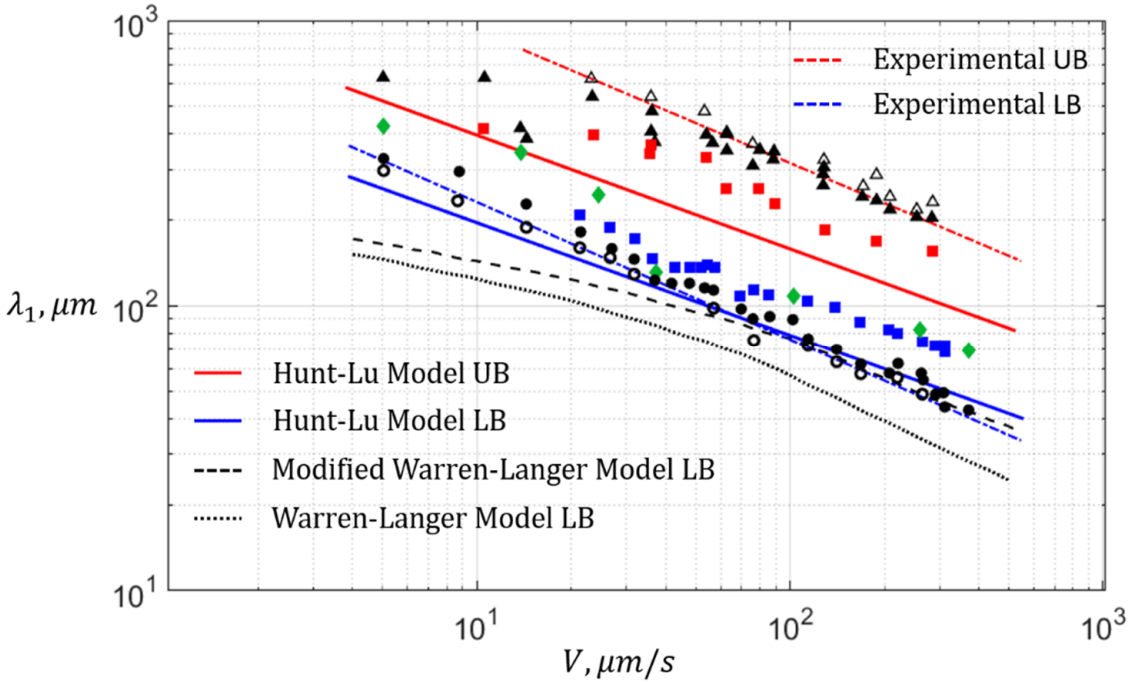

Figure 8. The allowable distribution of primary spacing, λ_1, within a succinonitrile-1.0 wt% acetone dendritic array, thermal gradient $= 4.0\ K/mm$ [115]. (Δ) critical λ_1 before tertiary arm branching; (▲) maximum stable λ_1; (○) critical λ_1 before overgrowth; (•) minimum stable λ_1; (■), (♦) and (■)—average λ_1 from step-increasing, constant and step-decreasing pulling velocity, respectively; UB—upper λ_1 bound; LB—Lower λ_1 bound. Plot adapted from [104].

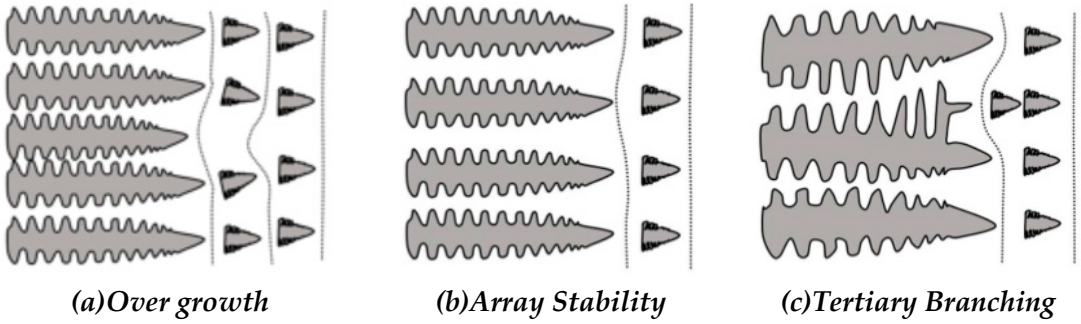

Figure 9. Schematic illustration of spacing adjustment mechanism for dendrites. Dotted line indicates the liquidus isotherm. Schematic adapted from [107].

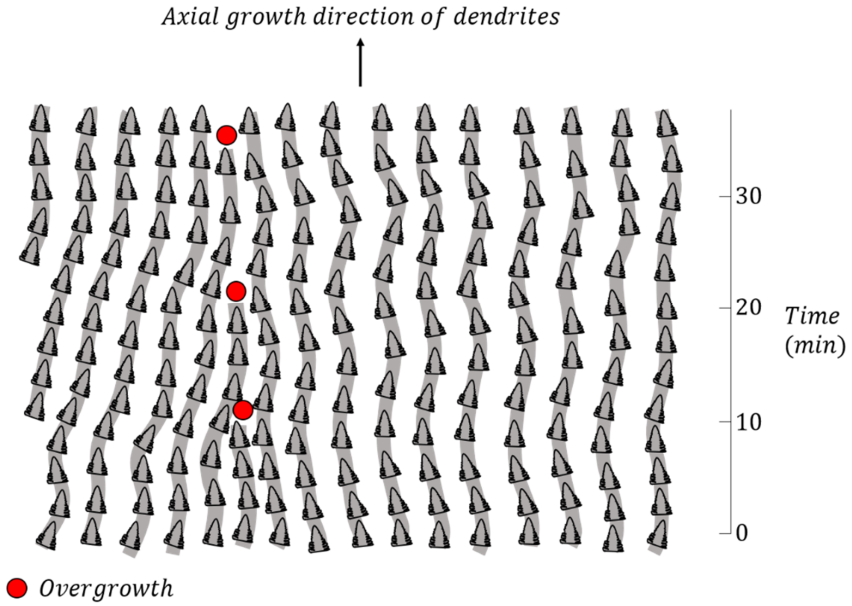

Figure 10. A schematic of real dendritic tip positions in an array as a function of time. Schematic adapted from [48].

3.7. Delimiting the Wide Range of Stable Primary Spacings

In 1996, Gandin et al. [41] noticed the upper λ_1 stability limit still required a proper theoretical treatment in order to delimit the wide range of possible spacings [115,117,118]; clearly illustrated in Figure 8. They recognised that most prior λ_1 models ignored the effect of local misorientation, side branch formation, and tertiary arm growth between neighbouring dendrites. This is important, as tertiary arm branching determines the upper stable λ_1 before the growth of a new primary dendrite (Figure 11). Gandin et al. developed a simple analytical model based on dynamic side branch formation using the parabolic dendrite growth model [39,72,111] to compute the $V-R$ and $V-\Delta T$ relations of secondary and tertiary branches. They applied secondary arm scaling laws as proposed by Esaka et al. [119] and Somboonsuk et al. [93], and used an experimentally determined exponent by Huang and Glicksman [66] for the active branches below the dendrite tip. Their model was as follows:

$$\lambda_1 \propto \Delta T_0^a V^{-b} G^{-c} F(\theta), \tag{19}$$

where,

$$F(\theta) = 1 + d\left[(cos\theta)^{-e} - 1\right], \tag{20}$$

and $a = b = 0.25$, $c = 0.5$, $d = 0.15$, $e = 8$ and θ is the angle between the misorientated primary dendrite trunk and the thermal direction (Figure 11). The analytical branching-based model illustrates the trends of primary spacing evolution with orientation for different imposed values of G and V. It was the first quantitative approach to evaluate the λ_1 based on the tertiary arm mechanism and emphasised the concepts required in developing a branching limited primary spacing evolution theory. However, their approach was limited to applications at locally misorientated boundaries (Figure 11) and provides only a measure of the influence of local misorientation on upper λ_1 selection.

Losert et al. [117,120,121] investigated quantitatively the linear stability analysis of Warren and Langer [102,103] and their prediction of spatial period-doubling bifurcation. Using SCN doped with 0.43 wt% of the laser dye coumarin 152, these researchers set up a steady state uniformly spaced array and slowly reduced the V_p until the array became unstable (Figure 12). They observed, in the central region of the sample, every other dendrite falling back, and a doubling of the interdendritic spacing (Figure 12b). Immediately after the doubling, there was a large distribution of λ_1 which then proceeded to decrease by the lateral adjustment mechanism [48] (Figure 10). Losert et al. concluded

that a steady state dendritic array of given λ_1 (Figure 12a) is stable over a wide range of V_p with a lower stability bound determined by the spatial period-doubling instability (Figure 12b). Furthermore, the same instability sets the lower bound for an array of different λ_1 for a fixed V_p.

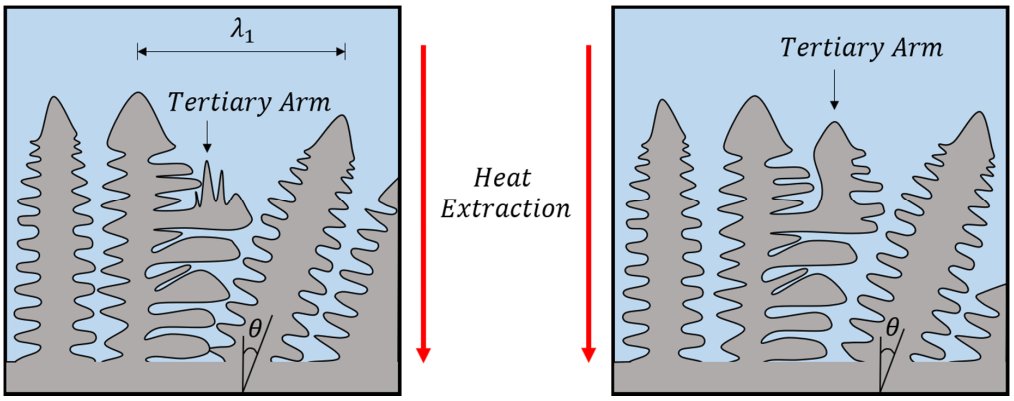

Figure 11. Tertiary side branch formation leading to a new primary dendrite at a divergent grain boundary. The larger the local misorientation angle, θ, the larger the local λ_1. Schematic adapted from [41].

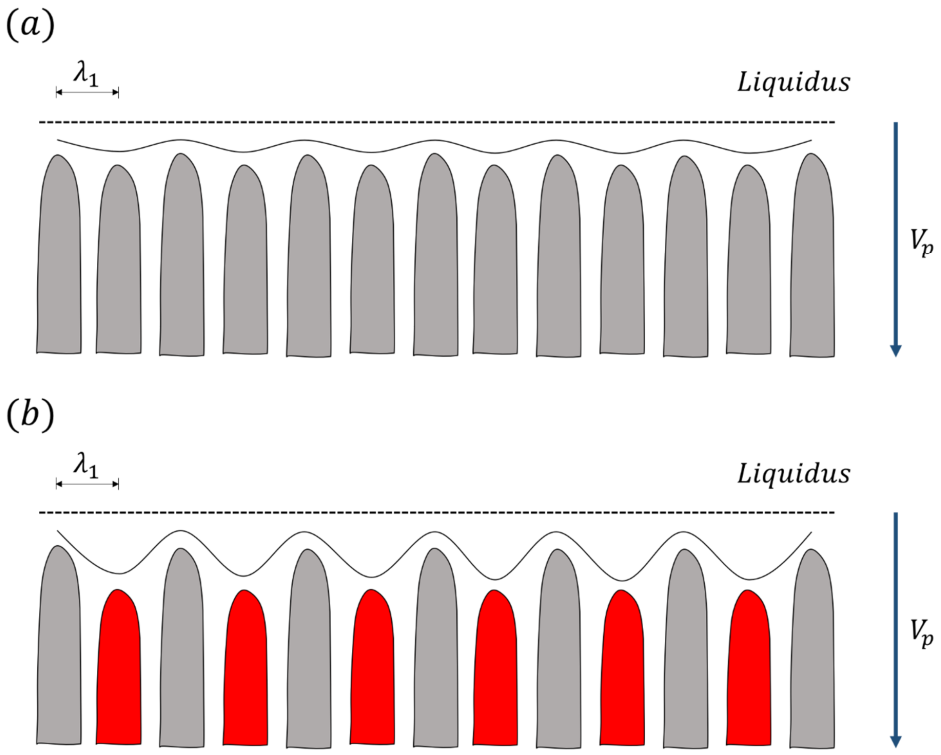

Figure 12. (**a**) An array of fixed λ_1 stable for a range of pulling velocities, V_p. (**b**) At some critical V_p, the spatial period-doubling instability occurs, which results in the removal of every other cell/dendrite (red) and a doubling of λ_1. Schematic adapted from [117].

3.8. Models Viewed as Complimentary to Hunt and Lu

In 1997, Bouchard and Kirkaldy (B–K) [50,122] developed a numerical model to characterise λ_1 for unsteady (ingot solidification) and steady state (directional solidification) heat flow conditions. These researchers were interested in unsteady state heat flow conditions as this type of solidification encompasses most industrial processes. Their model is derived for two-dimensional cells from an earlier semi-empirical heuristically developed steady state formula [123], which after modification, demonstrated its utility in the unsteady regime:

$$\lambda_1 = \alpha_1 \left(\frac{16 C_0^{0.5} G_0 \varepsilon \Gamma D}{(1-k) m G V} \right)^{0.5}, \tag{21}$$

where, $G_0\varepsilon$ is a characteristic parameter $(600 \times 6\ K/cm)$; α_1 is the primary spacing calibrating factor. The model demonstrated a reasonable fit with a variety of binary alloy data but required α_1 to account for some uncertainties. B–K suggested that Equation (21) could be used to predict λ_1 within binary alloys when experimental data was lacking, however, a prior knowledge of G and V at the dendrite tip is required.

In 1997, Spencer and Huppert (S–H) [124,125] developed a branchless λ_1 model to predict morphology characteristics of dendrite growth, such as R, λ_1, ΔT and overall dendrite shape. These researchers analysed different morphological and experimental length scales from the results of Somboonsuk et al. [93]. From this they noticed a natural separation and identified a characteristic small parameter to describe dendritic growth. S–H solved numerically asymptotic equations to derive an integral equation for the shape of a dendrite by considering nonlinear interactions between neighbouring dendrites and then solving for the nontrivial details of the shape. Iconoclastically, they were able to obtain a unique solution for the shape without considering sidebranches or a selection criterion based on surface energy. For a given set of experimental conditions, their integral equation had a family of solutions parameterised only by the λ_1 of the array. S–H determined the lower λ_1 by the Warren and Langer overgrowth condition [102] and the upper λ_1 by marginal stability [68,69]. Their model could not determine which λ_1 is observed in practice as the actual λ_1 is intrinsically time and history dependent [48,103,114]. The model was offered as an alternative view to the traditionally accepted theory of microscopic solvability and was demonstrated relevant at moderate growth V, where surface energy effects are negligible.

In 1998, Ma and Sahm (M–S) [40] developed a simple analytical model to provide a description of the variation in λ_1 as a function of V. M-S separated the dendritic envelope into a centre core and its sidearms (Figure 13), on the basis that the inclusion of sidearms are absent from the Hunt–Lu analysis [49]. M–S applied a simple relationship between the tip diameter, $(\varnothing = 2 \times R)$, and the side arm length, S to determine λ_1 (Figure 13). To calculate R for a given growth condition M–S used the marginal stability criterion [68,69]. To determine S they calculated a 'free growth coefficient', g_s, which characterised the proportion of the free growth of the side arms compared with the entire solidification time. They determined g_s as a function of system properties and processing parameters based on theoretical reasoning and careful study of experimental variables. The researchers derived equations for:

cellular growth $(S = 0)$,

$$\lambda_1 = 4\pi \left(\frac{D\Gamma}{k \Delta T_0} \right)^{0.5} \left(1 - \frac{V_c}{V} \right)^{-0.5} V^{-0.5}, \tag{22}$$

and dendritic growth $(S > 0)$,

$$\lambda_1 = 2\pi (kD\Gamma \Delta T_0)^{0.25} \left(1 - \frac{V_c}{V} \right)^{0.75} G^{-0.5} V^{-0.25}. \tag{23}$$

M–S compared their model with the analytical expression of Hunt and Lu [49] over several alloy systems. When compared with cellular growth experimental data, both models demonstrated a reasonable fit. However, when applied to the moderate V dendritic growth regime, the Ma and Sahm model appeared to be making better predictions than the more rigorously derived steady state theory of Hunt and Lu.

In 2002, Ma [126] developed an analytical model to describe the typical features of primary spacing selection, such as delayed response of λ_1 variation, the wide range in λ_1 distribution, and λ_1 history-dependence. The motivation behind this work was the absence of a model of tertiary arm

branching in a dendritic array of the same orientation. The model was developed for constrained growth using scaling laws [93,97] and marginal stability [68]. Ma determined a nominal λ_1 that provided the steady state baseline for the average array λ_1 and developed kinetic factors for the overgrowth and branching limits. The variation in array λ_1 was described by a beta distribution, which provided a sharp lower and upper λ_1 limit. Following the same procedure as Huang et al. [114], Ma step-increased the V_p within the model. When the local λ_1 was larger than a critical branching limit, new primary dendrites formed and the average array λ_1 updated. The model was then applied to a step-decreasing V_p, dendrites whose λ_1 were below the critical overgrowth limit were eliminated. The model showed an excellent fit with the history-dependant results of Huang et al. [114] (Figure 14). It could quantitatively calculate the minimum, maximum and average λ_1 in response to a change in V from an initial stage of stable growth. Following this, Ma [127] extended the model to predict the λ_1 distribution with varying G, whilst the V remained constant. The results between both analytical models demonstrated the same intrinsic λ_1 relationship and a good fit with experimental data [114].

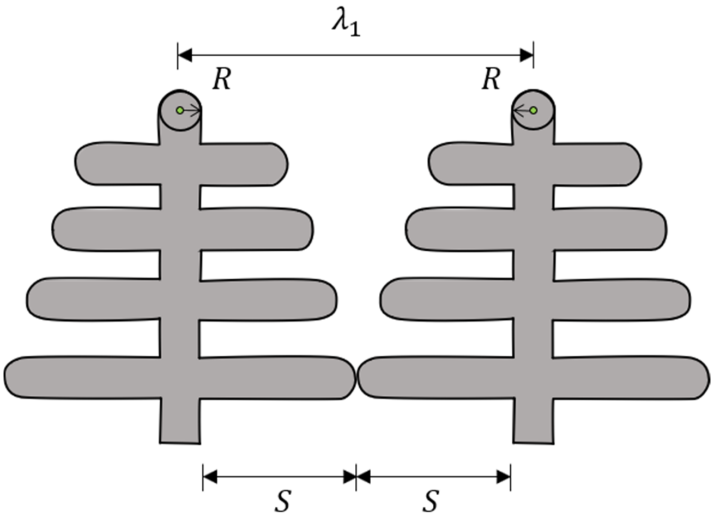

Figure 13. The λ_1 is the sum of the side lengths plus the dendrite core diameter ($\varnothing = 2 \times R$).

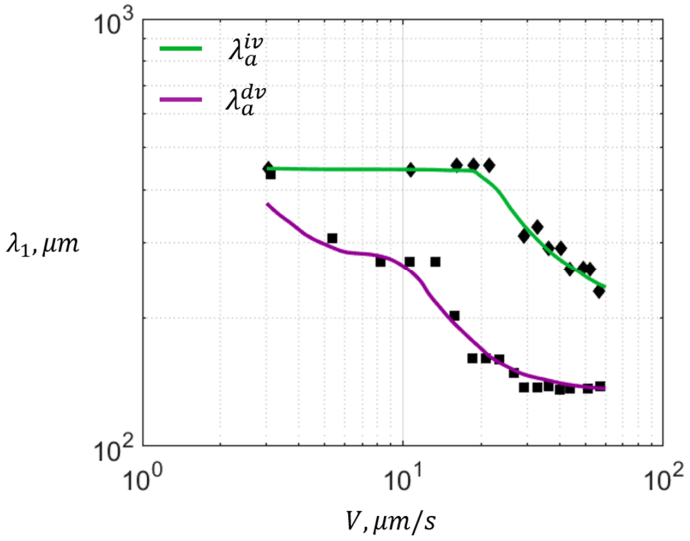

Figure 14. Average λ_1 predicted by the Ma model for increasing, λ_a^{iv}, and decreasing, λ_a^{dv}, pulling velocity. The model is compared with the average λ_1 experimental data for increasing and decreasing pulling velocity from Huang et al. [114]. Thermal gradient fixed at 4.8 K/mm. Plot adapted from [126].

4. Dendritic Growth Computational Modelling—Present Day

The unstable and complex morphological nature of the solid–liquid interface has been a considerable challenge for the implementation of suitable analytical and numerical models that can adequately describe primary spacing distribution as a function of the process variables. Currently, the lower stability bound for a fixed set of growth conditions has received a proper theoretical treatment and is predicted analytically [103] and numerically [107] with good accuracy (Figure 8). The upper stability bound is understood from an analytical point of view [41,126,127]. Unfortunately, the mechanisms behind local dendritic misorientation and its influence on the upper λ_1 selection procedure are not fully understood. Multiple investigation into the origins of misorientation have identified plastic deformation through differential thermal contraction in the mushy zone as the probable cause of dendritic bending [128–138]. However, to the authors' knowledge, no proper analytical or numerical treatment of the driving force behind dendritic bending or its influence on the upper primary selection procedure is reported in the literature. In addition to this, the mechanisms behind the history-dependent λ_1 selection and the stable λ_1 distribution for a given set of growth conditions are unknown. Consequently, accurate prediction of the severity of defect formation, the homogenisation times, and mechanical properties within a material, are not currently possible.

Now, the problem with applying purely diffusion-limited models to study directional dendritic array growth is the assumption of a 'convection free' environment where an isoconcentrate exists ahead of the growing solidification front. In a situation where convective effects are minimised, such as in thin samples, low Péclet number materials, and in microgravity, a steady state approach such as that of Hunt and Lu [107] may be appropriate. However, within constrained 3D dendritic growth, unsteady state heat flow conditions, natural convection, and macrosegregation can occur, significantly influencing the final microstructural patterns [39,139–144]. Unfortunately, the presence of density variations within the melt drives convective heat and mass transport. Due to the added length and time scales, microstructural patterns can differ greatly from those generated using purely heat and mass transfer [145]. The influence of thermosolutal convection within the melt can trigger unexpected and complicated flow phenomena. The resultant redistribution of heat and mass significantly influence the growth of the solidifying dendritic array, leading to macrosegregation within the solidified crystal and array disorder [39]. Fortunately, in the last 20 years, substantial increases in computational power have permitted the development of more complex modelling methods, enabling the full dendrite growth problem including convective effects to be studied. The two most popular techniques are the Cellular Automata (CA) and Phase Field (PF) methods. The purpose of the following section is to provide a very brief overview on the recent applications of modelling and highlight its expanding role within the field of solidification science.

CA has found application in realistic computation at the micro-macroscopic scale with moderate demand for computation (Figure 15). It offers a balance between computational efficiency and physically reasonable rules for modelling solidification of a domain. CA works by combining analytical microscopic dendritic growth models (e.g., LGK [146] or KGT [147]), with numerical models for heat and mass transport at the scale of grains. It is now fully coupled with momentum, mass and energy transportation in liquid, solid and mushy zones [148,149]. Models derived from CA approaches such as Cellular Automata Finite Difference (CAFD) have simulated the evolution of dendritic morphology during alloy solidification in the presence of melt convection [150–152], stray grain formation [153,154], multiscale modelling [155], geometry-related grain boundary formation [156], freckle formation [157] and multi-component systems [158,159]. However, a major challenge with this method is the substantial anisotropic influence of the underlying grid on the simulation results [160]. The grid anisotropy superposes the physical anisotropy and therefore impedes the interpretation of the simulated microstructure; currently restricting CA simulation to a qualitative representation of dendritic solidification.

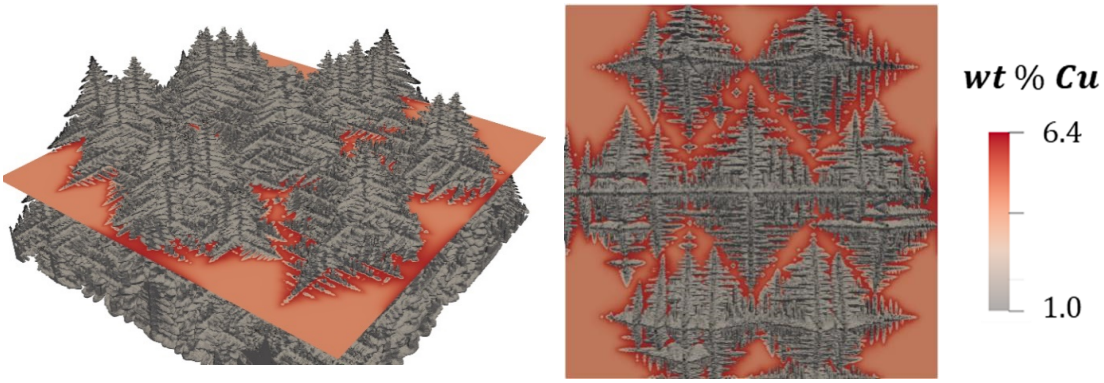

Figure 15. Cellular Automata Finite Difference (CAFD) model of hexagonally packed $Al-4.5\ wt\%\ Cu$ dendrites. Tip undercooling, 4 K; thermal gradient, 1 K/mm; growth velocity 0.7 mm/s. The crystals were grown using the Dong et al. [161] methodology.

PF is constructed from basic thermodynamical and fundamental conservational laws and has a phenomenological character. It has developed into an important and extremely versatile technique for simulating microstructure evolution at the micro-mesoscale. The PF method possesses a significantly higher resolution of both the simulation domain as a whole and the solid–liquid interface than CA; thus, generating a substantially lower anisotropic error. PF can compute realistic and complex interface shapes associated with dendritic growth without making any a priori assumptions on the shape of the grains (Figure 16). Owing to this, PF has helped validate the microscopic solvability theory [162] and has successfully simulated a wide range of solidification and interfacial pattern formation phenomena, such as, grain growth competition [163–165] at divergent [166,167] and convergent [168,169] boundaries, spacing evolution [34,170], pattern selection [38,171–178], side branching [179], convection [145,149,180], rapid solidification [181–185] and multiphase and multicomponent systems [186–200]. In the last decade, microstructures at physically relevant length and time scales in 3D [201–204] have been simulated using advanced GPU's. However, as PF models deal with a large number of complex nonlinear terms, even with parallel architectures [202], currently only a few hundred columnar dendrites formed in diffusive conditions have been simulated [203].

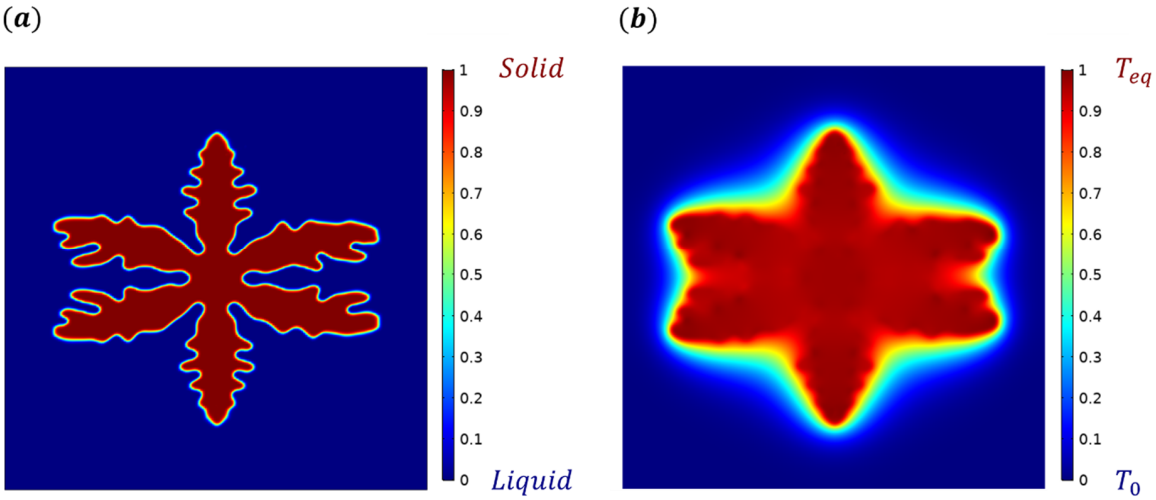

Figure 16. (**a**) A Phase Field model of the solidification of a hexagonal anisotropy crystal. (**b**) Dimensionless temperature variation generated from the latent heat of (**a**); T_0 is the characteristic cooling temperature; T_{eq} is the equilibrium temperature. The crystal was grown using the Kobayashi dimensionless model with $\delta = 0.040$ and $K = 2$ [205].

5. Dendritic Growth in Metallic Alloy Systems—Synchrotron X-ray and Neutron Source

Accurate prediction of constrained 3D metallic array growth with analytical or numerical primary spacing models, CA or PF is difficult. These models contain mathematical simplifications, assumptions, conjectures, or phenomenological parameters that are determined from either theoretical information or analogue experimental data. Application of organic analogues in microgravity has validated the diffusion theory of dendritic growth [83–88] and elucidated the constrained 3D array growth behaviour under diffusive conditions [172,206–211]. Unfortunately, analogues cannot accurately represent the growth of a solidifying metal as they have different interfacial energies, diffusion coefficients, heat capacities, thermal conductivities, and chemical potentials. Over the last twenty years, two important experimental types have come to the forefront as fundamental tools for studying metallic systems. These techniques take advantage of the penetrating nature of synchrotron and neutron radiation for investigation into material structure and property.

Synchrotron X-ray experiments have helped validate numerical and computational modelling efforts of metal alloys [212–216]. They have provided quantitative data to test theory [217–220], however, the low penetration depth of X-rays within metals has limited synchrotron X-ray analysis to only a few hundred microns [221]; enough volume for investigation into the growth of a few metallic dendrites. It is hoped that the development of fourth-generation synchrotron light sources with multi-bend achromat synchrotron storage rings and free-electron lasers, will improve the brightness and coherent fraction of the x-ray light, whilst shortening the pulse duration [222]. However, to translate the progress in light source quality into improvements in wavelength resolution, spatio-temporal limits, and new science, requires similar progress in aspects such as X-ray optics, sample preparation, beamline technology, data analysis, and detectors [223]. Synchrotron sources have the potential to make great contributions in understanding the mechanisms behind pattern formation in constrained growth metallic alloy systems. However, to exploit them, the full technology from source to detector must first be developed to increase voxel size and enable the investigation of larger dendritic arrays.

More recently, there has been a revived interest in neutron imaging due to improvements in computer processors and bus speeds, large fast data storage devices, CCD imaging chip development and low-light cameras. Although neutron imaging cannot compete with X-rays in terms of spatial or temporal resolution [224–226], they are especially good at probing objects made from heavier elements and can penetrate thick component sections enabling investigation of bulk material characteristics. Recently, a micro channel plate (MCP) detector was combined with a Medipix2/Timepix readout which improved neutron spatial resolution from 2 mm to 55 μm [227,228] for a field of view of several square centimetres. Following this, multiple new imaging and diffraction methods have been developed to investigate the shape and orientation of grains [224,229,230]. The spatial resolution of the MCP detector is now nearly ten times smaller than the typical λ_1 length [231,232]. Therefore, neutron imaging may provide the micro-macroscopic experimental link for improving understanding of the process versus property relationships within directionally solidified bulk metallic alloys.

6. Outlook

This review summarises the important aspects of directional dendritic growth and primary spacing selection within the past 85 years. In this time, there have been significant developments in understanding the dendritic growth problem. Extensive theoretical and experimental studies have established criterion by which dendrite tip radius is selected under given experimental conditions. This paved the way for analytical and numerical models of primary spacing evolution and the confirmation of the diffusion part of the dendrite growth theory. More recently, the Cellular Automata (CA) and Phase Field (PF) techniques have enabled study of the influence of convection on dendrite growth evolution. Complimentary synchrotron X-ray and neutron radiation experiments have enabled quantitative testing of theory and numerical modelling on metallic alloy systems. In the authors' opinion, constrained growth research should focus on:

- providing a proper theoretical treatment of the mechanism/s behind the upper primary spacing stability bound under 3D growth conditions;
- determining the reason behind the history dependence of primary spacing distribution for a given set of growth conditions;
- investigating 3D lateral translation and providing a mechanism behind this phenomenon;
- understanding the relationship between strain and misorientation;
- quantifying the influence of convection within the melt on primary spacing variation;
- comparing microgravity experiments and PF modelling of diffusive directional dendritic growth with identical terrestrial experiments;
- reducing the influence of grid anisotropy in CA to enable quantitative modelling of micro-macroscopic scale phenomena;
- improving computational efficiency of PF modelling to facilitate larger scale simulations with convective melt flow;
- utilising synchrotron X-ray and neutron sources for further investigation into directional dendritic growth theory and ascertaining metallic phenomenological parameters.

Author Contributions: Conceptualisation, investigation, and writing—original draft presentation, J.S.; writing—review and editing, B.N.; supervision and funding acquisition, H.D. All authors have read and agreed to the published version of the manuscript.

Funding: This research and the APC was funded by EPRSC grant number EP/L016206/1.

Acknowledgments: J.S. and B.N. wish to acknowledge EPSRC CDT (Grant No: EP/L016206/1) in Innovative Metal Processing for providing PhD studentships for this study and Rolls-Royce Plc for providing financial support. The authors would also like to thank Jun Li and the reviewers for providing insightful comments for the manuscript revision.

Conflicts of Interest: The authors declare no conflict of interest.

References

1. Ivantsov, G. Diffusion Supercooling during the Solidification of a Binary Alloy. *Dokl. Akad. Nauk SSSR* **1951**, *81*, 179–182.
2. Tiller, W.; Jackson, K.; Rutter, J.; Chalmers, B. The redistribution of solute atoms during the solidification of metals. *Acta Metall.* **1953**, *1*, 428–437. [CrossRef]
3. Singer, H. Measurements of the three-dimensional shape of ice crystals in supercooled water. *Phys. Rev. E* **2006**, *73*, 051606. [CrossRef]
4. McCartney, D.; Hunt, J. Measurements of cell and primary dendrite arm spacings in directionally solidified aluminium alloys. *Acta Metall.* **1981**, *29*, 1851–1863. [CrossRef]
5. D'Souza, N.; Beanland, R.; Hayward, C.; Dong, H. Accuracy of composition measurement using X-ray spectroscopy in precipitate-strengthened alloys: Application to Ni-base superalloys. *Acta Mater.* **2011**, *59*, 1003–1013. [CrossRef]
6. D'souza, N.; Dong, H. Solidification path in third-generation Ni-based superalloys, with an emphasis on last stage solidification. *Scr. Mater.* **2007**, *56*, 41–44. [CrossRef]
7. Dong, H.; Wang, W.; Lee, P.D. Simulation of the thermal history dependence of primary spacing during directional solidification. *Superalloys 2004* **2004**, 925–931. Available online: https://pdfs.semanticscholar.org/887e/23d1e65f07b748e0289c7f4b40d321a7162f.pdf (accessed on 20 July 2020).
8. Welton, D.; D'Souza, N.; Kelleher, J.; Gardner, S.; Dong, Z.; West, G.; Dong, H. Discontinuous precipitation in Ni-base superalloys during solution heat treatment. *Metall. Mater. Trans. A* **2015**, *46*, 4298–4315. [CrossRef]
9. Pang, H.T.; D'Souza, N.; Dong, H.; Stone, H.J.; Rae, C.M. Detailed Analysis of the Solution Heat Treatment of a Third-Generation Single-Crystal Nickel-Based Superalloy CMSX-10K®. *Metall. Mater. Trans. A* **2016**, *47*, 889–906. [CrossRef]
10. Brundidge, C.; Van Drasek, D.; Wang, B.; Pollock, T. Structure refinement by a liquid metal cooling solidification process for single-crystal nickel-base superalloys. *Metall. Mater. Trans. A* **2012**, *43*, 965–976. [CrossRef]

11. Hui, J.; Tiwari, R.; Wu, X.; Tewari, S.N.; Trivedi, R. Primary dendrite distribution and disorder during directional solidification of Pb-Sb alloys. *Metall. Mater. Trans. A* **2002**, *33*, 3499–3510. [CrossRef]
12. Zhao, X.; Liu, L.; Yu, Z.; Zhang, W.; Zhang, J.; Fu, H. Influence of directional solidification variables on the microstructure and crystal orientation of AM3 under high thermal gradient. *J. Mater. Sci.* **2010**, *45*, 6101–6107. [CrossRef]
13. Zhang, W.; Liu, L. Solidification microstructure of directionally solidified superalloy under high temperature gradient. *Rare Met.* **2012**, *31*, 541–546. [CrossRef]
14. Trivedi, R.; Mason, J. The effects of interface attachment kinetics on solidification interface morphologies. *Metall. Trans. A* **1991**, *22*, 235–249. [CrossRef]
15. Liu, L.; Huang, T.; Qu, M.; Liu, G.; Zhang, J.; Fu, H. High thermal gradient directional solidification and its application in the processing of nickel-based superalloys. *J. Mater. Process. Technol.* **2010**, *210*, 159–165. [CrossRef]
16. Ramsperger, M.; Singer, R.F.; Körner, C. Microstructure of the nickel-base superalloy CMSX-4 fabricated by selective electron beam melting. *Metall. Mater. Trans. A* **2016**, *47*, 1469–1480. [CrossRef]
17. Wang, F.; Ma, D.; Zhang, J.; Bogner, S.; Bührig-Polaczek, A. A high thermal gradient directional solidification method for growing superalloy single crystals. *J. Mater. Process. Technol.* **2014**, *214*, 3112–3121. [CrossRef]
18. Brundidge, C.; Miller, J.; Pollock, T. Development of dendritic structure in the liquid-metal-cooled, directional-solidification process. *Metall. Mater. Trans. A* **2011**, *42*, 2723–2732. [CrossRef]
19. Rezaei, M.; Kermanpur, A.; Sadeghi, F. Effects of withdrawal rate and starter block size on crystal orientation of a single crystal Ni-based superalloy. *J. Cryst. Growth* **2018**, *485*, 19–27. [CrossRef]
20. Lamm, M.; Singer, R. The effect of casting conditions on the high-cycle fatigue properties of the single-crystal nickel-base superalloy PWA 1483. *Metall. Mater. Trans. A* **2007**, *38*, 1177–1183. [CrossRef]
21. Wilson, B.; Cutler, E.; Fuchs, G. Effect of solidification parameters on the microstructures and properties of CMSX-10. *Mater. Sci. Eng. A* **2008**, *479*, 356–364. [CrossRef]
22. Quaresma, J.M.; Santos, C.A.; Garcia, A. Correlation between unsteady-state solidification conditions, dendrite spacings, and mechanical properties of Al-Cu alloys. *Metall. Mater. Trans. A* **2000**, *31*, 3167–3178. [CrossRef]
23. Goulart, P.R.; Spinelli, J.E.; Osório, W.R.; Garcia, A. Mechanical properties as a function of microstructure and solidification thermal variables of Al–Si castings. *Mater. Sci. Eng. A* **2006**, *421*, 245–253. [CrossRef]
24. Osorio, W.R.; Goulart, P.R.; Garcia, A.; Santos, G.A.; Neto, C.M. Effect of dendritic arm spacing on mechanical properties and corrosion resistance of Al 9 Wt Pct Si and Zn 27 Wt Pct Al alloys. *Metall. Mater. Trans. A* **2006**, *37*, 2525–2538. [CrossRef]
25. Whitesell, H.; Overfelt, R. Influence of solidification variables on the microstructure, macrosegregation, and porosity of directionally solidified Mar-M247. *Mater. Sci. Eng. A* **2001**, *318*, 264–276. [CrossRef]
26. Elliott, A.; Pollock, T.; Tin, S.; King, W.; Huang, S.-C.; Gigliotti, M. Directional solidification of large superalloy castings with radiation and liquid-metal cooling: A comparative assessment. *Metall. Mater. Trans. A* **2004**, *35*, 3221–3231. [CrossRef]
27. Melo, M.; Rizzo, E.; Santos, R. Predicting dendrite arm spacing and their effect on microporosity formation in directionally solidified Al-Cu alloy. *J. Mater. Sci.* **2005**, *40*, 1599–1609. [CrossRef]
28. Yue, Q.; Liu, L.; Yang, W.; Huang, T.; Zhang, J.; Fu, H.; Zhao, X. Influence of withdrawal rate on the porosity in a third-generation Ni-based single crystal superalloy. *Prog. Nat. Sci. Mater. Int.* **2017**, *27*, 236–243. [CrossRef]
29. Yang, X. Simulation of Stray Grain Formation in Single Crystal Ni-Based Superalloy Turbine Blades. Ph.D. Thesis, Imperial College London (University of London), London, UK, 2005.
30. Giamei, A.F.; Kear, B. On the nature of freckles in nickel base superalloys. *Metall. Trans.* **1970**, *1*, 2185–2192. [CrossRef]
31. Matache, G.; Stefanescu, D.; Puscasu, C.; Alexandrescu, E. Dendritic segregation and arm spacing in directionally solidified CMSX-4 superalloy. *Int. J. Cast Met. Res.* **2016**, *29*, 303–316. [CrossRef]
32. Stanford, N.; Djakovic, A.; Shollock, B.; McLean, M.; D'Souza, N.; Jennings, P. Defect grains in the melt-back region of CMSX-4 single crystal seeds. *Superalloys* **2004**, *2004*, 719–726.
33. Tiryakioğlu, M. On the statistical distribution of primary and secondary dendrite arm spacing in cast metals. *Mater. Sci. Technol.* **2019**, *35*, 509–511. [CrossRef]
34. Ghosh, S.; Ma, L.; Ofori-Opoku, N.; Guyer, J.E. On the primary spacing and microsegregation of cellular dendrites in laser deposited Ni–Nb alloys. *Model. Simul. Mater. Sci. Eng.* **2017**, *25*, 065002. [CrossRef]

35. Santos, G.; Goulart, P.R.; Couto, A.A.; Garcia, A. Primary dendrite arm spacing effects upon mechanical properties of an Al–3wt% cu–1wt% li alloy. In *Properties and Characterization of Modern Materials*; Springer: Singapore, 2017; pp. 215–229.
36. Tschopp, M.A.; Miller, J.D.; Oppedal, A.L.; Solanki, K.N. Evaluating local primary dendrite arm spacing characterization techniques using synthetic directionally solidified dendritic microstructures. *Metall. Mater. Trans. A* **2015**, *46*, 4610–4628. [CrossRef]
37. Tschopp, M.A.; Miller, J.D.; Oppedal, A.L.; Solanki, K.N. Characterizing the local primary dendrite arm spacing in directionally solidified dendritic microstructures. *Metall. Mater. Trans. A* **2014**, *45*, 426–437. [CrossRef]
38. Wang, Z.; Li, J.; Wang, J.; Zhou, Y. Phase field modeling the selection mechanism of primary dendritic spacing in directional solidification. *Acta Mater.* **2012**, *60*, 1957–1964. [CrossRef]
39. Trivedi, R.; Mazumder, P.; Tewari, S. The effect of convection on disorder in primary cellular and dendritic arrays. *Metall. Mater. Trans. A* **2002**, *33*, 3763–3775. [CrossRef]
40. Ma, D.; Sahm, P.R. Primary spacing in directional solidification. *Metall. Mater. Trans. A* **1998**, *29*, 1113–1119. [CrossRef]
41. Gandin, C.A.; Eshelman, M.; Trivedi, R. Orientation dependence of primary dendrite spacing. *Metall. Mater. Trans. A* **1996**, *27*, 2727–2739. [CrossRef]
42. Ivantsov, G. Temperature field around a spherical, cylindrical, and needle-shaped crystal, growing in a pre-cooled melt. *Dokl. Akad. Nauk SSSR* **1947**, *58*, 567–569.
43. Temkin, D. Growth rate of the needle-crystal formed in a supercoled melt. *Dokl. Akad. Nauk SSSR* **1960**, *132*, 1307–1310.
44. Amar, M.B.; Pomeau, Y. Theory of dendritic growth in a weakly undercooled melt. *EPL* **1986**, *2*, 307. [CrossRef]
45. Hunt, J.D. *Solidification and Casting of Metals*; The Metals Society: London, UK, 1979; pp. 3–9.
46. Kurz, W.; Fisher, D. Dendrite growth at the limit of stability: Tip radius and spacing. *Acta Metall.* **1981**, *29*, 11–20. [CrossRef]
47. Trivedi, R. Interdendritic spacing: Part II. A comparison of theory and experiment. *Metall. Mater. Trans. A* **1984**, *15*, 977–982. [CrossRef]
48. Han, S.H.; Trivedi, R. Primary spacing selection in directionally solidified alloys. *Acta Metall. Mater.* **1994**, *42*, 25–41. [CrossRef]
49. Hunt, J.; Lu, S.-Z. Numerical modeling of cellular/dendritic array growth: Spacing and structure predictions. *Metall. Mater. Trans. A* **1996**, *27*, 611–623. [CrossRef]
50. Bouchard, D.; Kirkaldy, J.S. Prediction of dendrite arm spacings in unsteady-and steady-state heat flow of unidirectionally solidified binary alloys. *Metall. Mater. Trans. B* **1997**, *28*, 651–663. [CrossRef]
51. Kurz, W.; Fisher, D.J.; Trivedi, R. Progress in modelling solidification microstructures in metals and alloys: Dendrites and cells from 1700 to 2000. *Int. Mater. Rev.* **2019**, *64*, 311–354. [CrossRef]
52. Kurz, W.; Rappaz, M.; Trivedi, R. Progress in modelling solidification microstructures in metals and alloys. Part II: Dendrites from 2001 to 2018. *Int. Mater. Rev.* **2020**, 1–47. Available online: https://iom3.tandfonline.com/action/doSearch?AllField=2020&SeriesKey=yimr20&pageSize=10&subjectTitle=&startPage=2 (accessed on 16 July 2020). [CrossRef]
53. Papapetrou, A. Untersuchungen über dendritisches Wachstum von Kristallen. *Z. für Krist.-Cryst. Mater.* **1935**, *92*, 89–130. [CrossRef]
54. Horvay, G.; Cahn, J. Dendritic and spheroidal growth. *Acta Metall.* **1961**, *9*, 695–705. [CrossRef]
55. Zener, C. Kinetics of the decomposition of austenite. *Trans. AIME* **1946**, *167*, 550–595.
56. Hillert, M. The role of interfacial energy during solid-state phase transformations. *Jernkontorets Ann.* **1957**, *141*, 757–789.
57. Bolling, G.; Tiller, W. Growth from the melt. III. Dendritic growth. *J. Appl. Phys.* **1961**, *32*, 2587–2605. [CrossRef]
58. Kotler, G.; Tarshis, L. An extension to the analysis of dendritic growth in pure systems. *J. Cryst. Growth* **1969**, *5*, 90–98. [CrossRef]
59. Trivedi, R. Growth of dendritic needles from a supercooled melt. *Acta Metall.* **1970**, *18*, 287–296. [CrossRef]
60. Trivedi, R. The role of interfacial free energy and interface kinetics during the growth of precipitate plates and needles. *Metall. Trans.* **1970**, *1*, 921.

61. Nash, G.E. *Capillarity-Limited Steady-State Dendritic Growth. Part 1. Theoretical Development*; Naval Research Lab: Washington, DC, USA, 1974.
62. Jackson, K.; Hunt, J. Transparent compounds that freeze like metals. *Acta Metall.* **1965**, *13*, 1212–1215. [CrossRef]
63. Jackson, K.; Uhlmann, D.R.; Hunt, J. On the nature of crystal growth from the melt. *J. Cryst. Growth* **1967**, *1*, 1–36. [CrossRef]
64. Glicksman, M.; Schaefer, R.; Ayers, J. Dendritic growth-a test of theory. *Metall. Trans. A* **1976**, *7*, 1747–1759. [CrossRef]
65. Chopra, M.; Glicksman, M.; Singh, N. Dendritic solidification in binary alloys. *Metall. Trans. A* **1988**, *19*, 3087–3096. [CrossRef]
66. Huang, S.-C.; Glicksman, M. Overview 12: Fundamentals of dendritic solidification—I. Steady-state tip growth. *Acta Metall.* **1981**, *29*, 701–715. [CrossRef]
67. Oldfield, W. Computer model studies of dendritic growth. *Mater. Sci. Eng.* **1973**, *11*, 211–218. [CrossRef]
68. Langer, J.; Müller-Krumbhaar, J. Stability effects in dendritic crystal growth. *J. Cryst. Growth* **1977**, *42*, 11–14. [CrossRef]
69. Langer, J.; Müller-Krumbhaar, H. Theory of dendritic growth—I. Elements of a stability analysis. *Acta Metall.* **1978**, *26*, 1681–1687. [CrossRef]
70. Mullins, W.W.; Sekerka, R.F. Morphological stability of a particle growing by diffusion or heat flow. *J. Appl. Phys.* **1963**, *34*, 323–329. [CrossRef]
71. Mullins, W.W.; Sekerka, R. Stability of a planar interface during solidification of a dilute binary alloy. *J. Appl. Phys.* **1964**, *35*, 444–451. [CrossRef]
72. Trivedi, R.; Kurz, W. Dendritic growth. *Int. Mater. Rev.* **1994**, *39*, 49–74. [CrossRef]
73. Bensimon, D.; Pelcé, P.; Shraiman, B.I. Dynamics of curved fronts and pattern selection. *J. Phys.* **1987**, *48*, 2081–2087. [CrossRef]
74. Ben-Jacob, E.; Goldenfeld, N.; Langer, J.; Schön, G. Dynamics of interfacial pattern formation. *Phys. Rev. Lett.* **1983**, *51*, 1930. [CrossRef]
75. Brower, R.C.; Kessler, D.A.; Koplik, J.; Levine, H. Geometrical approach to moving-interface dynamics. *Phys. Rev. Lett.* **1983**, *51*, 1111. [CrossRef]
76. Meiron, D.I. Selection of steady states in the two-dimensional symmetric model of dendritic growth. *Phys. Rev. A* **1986**, *33*, 2704. [CrossRef]
77. Barbieri, A.; Hong, D.C.; Langer, J.S. Velocity selection in the symmetric model of dendritic crystal growth. *Phys. Rev. A* **1987**, *35*, 1802–1808. [CrossRef]
78. Pelce, P.; Pomeau, Y. Dendrites in the small undercooling limit. In *Dynamics of Curved Fronts*; Academic Press: Boston, UK, 1988; pp. 327–340.
79. Kessler, D.A.; Levine, H. Stability of Dendritic Crystals. *Phys. Rev. Lett.* **1986**, *57*, 3069–3072. [CrossRef]
80. Ben-Jacob, E.; Garik, P. The formation of patterns in non-equilibrium growth. *Nature* **1990**, *343*, 523. [CrossRef]
81. Muschol, M.; Liu, D.; Cummins, H. Surface-tension-anisotropy measurements of succinonitrile and pivalic acid: Comparison with microscopic solvability theory. *Phys. Rev. A* **1992**, *46*, 1038. [CrossRef]
82. Glicksman, M.; Winsa, E.; Hahn, R.; Lograsso, T.; Tirmizi, S.; Selleck, M. Isothermal dendritic growth—A proposed microgravity experiment. *Metall. Trans. A* **1988**, *19*, 1945–1953. [CrossRef]
83. LaCombe, J.; Koss, M.; Fradkov, V.; Glicksman, M. Three-dimensional dendrite-tip morphology. *Phys. Rev. E* **1995**, *52*, 2778. [CrossRef]
84. Glicksman, M.E.; Koss, M.B.; Bushnell, L.T.; Lacombe, J.C.; Winsa, E.A. Dendritic growth of succinonitrile in terrestrial and microgravity conditions as a test of theory. *ISIJ Int.* **1995**, *35*, 604–610. [CrossRef]
85. Glicksman, M.; Koss, M.; Winsa, E. Dendritic growth velocities in microgravity. *Phys. Rev. Lett.* **1994**, *73*, 573. [CrossRef]
86. Tennenhouse, L.; Koss, M.; LaCombe, J.; Glicksman, M. Use of microgravity to interpret dendritic growth kinetics at small supercoolings. *J. Cryst. Growth* **1997**, *174*, 82–89. [CrossRef]
87. Koss, M.; LaCombe, J.; Tennenhouse, L.; Glicksman, M.; Winsa, E. Dendritic growth tip velocities and radii of curvature in microgravity. *Metall. Mater. Trans. A* **1999**, *30*, 3177–3190. [CrossRef]
88. Lee, Y.-W.; Smith, R.N.; Glicksman, M.E.; Koss, M.B. Effects of buoyancy on the growth of dendritic crystals. *Annu. Rev. Heat Transf.* **1996**, *7*, 59–139. [CrossRef]

89. Bower, T.F.; Brody, H.; Flemings, M.C. Measurements of solute redistribution in dendritic solidification. *AIME Met. Soc. Trans.* **1966**, *236*, 624–634.
90. Burden, M.; Hunt, J. Cellular and dendritic growth. II. *J. Cryst. Growth* **1974**, *22*, 109–116. [CrossRef]
91. Trivedi, R. Theory of dendritic growth during the directional solidification of binary alloys. *J. Cryst. Growth* **1980**, *49*, 219–232. [CrossRef]
92. Mason, J.T.; Verhoeven, J.; Trivedi, R. Primary dendrite spacing I. Experimental studies. *J. Cryst. Growth* **1982**, *59*, 516–524. [CrossRef]
93. Somboonsuk, K.; Mason, J.; Trivedi, R. Interdendritic spacing: Part I. Experimental studies. *Metall. Mater. Trans. A* **1984**, *15*, 967–975. [CrossRef]
94. Venugopalan, D.; Kirkaldy, J. Theory of cellular solidification of binary alloys with applications to succinonitrile-salol. *Acta Metall.* **1984**, *32*, 893–906. [CrossRef]
95. Eshelman, M.; Seetharaman, V.; Trivedi, R. Cellular spacings—I. Steady-state growth. *Acta Metall.* **1988**, *36*, 1165–1174. [CrossRef]
96. Somboonsuk, K.; Trivedi, R. Dynamical studies of dendritic growth. *Acta Metall.* **1985**, *33*, 1051–1060. [CrossRef]
97. Trivedi, R.; Somboonsuk, K. Pattern formation during the directional solidification of binary systems. *Acta Metall.* **1985**, *33*, 1061–1068. [CrossRef]
98. Amar, M.B.; Moussallam, B. Absence of selection in directional solidification. *Phys. Rev. Lett.* **1988**, *60*, 317. [CrossRef] [PubMed]
99. Dombre, T.; Hakim, V. Saffman-Taylor fingers and directional solidification at low velocity. *Phys. Rev. A* **1987**, *36*, 2811. [CrossRef] [PubMed]
100. Quested, P.; McLean, M. Solidification morphologies in directionally solidified superalloys. *Mater. Sci. Eng.* **1984**, *65*, 171–180. [CrossRef]
101. Chopra, M.; Tewari, S. Growth-speed dependence of primary arm spacings in directionally solidified Pb-10 Wt Pct Sn. *Metall. Trans. A* **1991**, *22*, 2467–2474. [CrossRef]
102. Warren, J.A.; Langer, J. Stability of dendritic arrays. *Phys. Rev. A* **1990**, *42*, 3518. [CrossRef]
103. Warren, J.A.; Langer, J. Prediction of dendritic spacings in a directional-solidification experiment. *Phys. Rev. E* **1993**, *47*, 2702. [CrossRef]
104. Ding, G.; Huang, W.; Lin, X.; Zhou, Y. Prediction of average spacing for constrained cellular/dendritic growth. *J. Cryst. Growth* **1997**, *177*, 281–288. [CrossRef]
105. Hunt, J. A numerical analysis of time dependent isolated dendritic growth for conditions near the steady state. *Acta Metall. Mater.* **1990**, *38*, 411–418. [CrossRef]
106. Hunt, J. A numerical analysis of dendritic and cellular growth of a pure material investigating the transition from "array" to "isolated" growth. *Acta Metall. Mater.* **1991**, *39*, 2117–2133. [CrossRef]
107. Lu, S.-Z.; Hunt, J. A numerical analysis of dendritic and cellular array growth: The spacing adjustment mechanisms. *J. Cryst. Growth* **1992**, *123*, 17–34. [CrossRef]
108. McCartney, D.; Hunt, J. A numerical finite difference model of steady state cellular and dendritic growth. *Metall. Mater. Trans. A* **1984**, *15*, 983–994. [CrossRef]
109. Hunt, J.; McCartney, D. Numerical finite difference model for steady state cellular array growth. *Acta Metall.* **1987**, *35*, 89–99. [CrossRef]
110. Lu, S.-Z.; Hunt, J.; Gilgien, P.; Kurz, W. Cellular and dendritic growth in rapidly solidified Al Fe and Al Cu alloys. *Acta Metall. Mater.* **1994**, *42*, 1653–1660. [CrossRef]
111. Kurz, W.; Giovanola, B.; Trivedi, R. Theory of microstructural development during rapid solidification. *Acta Metall.* **1986**, *34*, 823–830. [CrossRef]
112. Hunt, J.; Thomas, R. Microscopical Modelling of Binary/Multicomponent Alloys. In Proceedings of the Fourth Decennial International Conference on Solidification Processing, Sheffield, UK, 7–10 July 1997.
113. Hunt, J. Pattern formation in solidification. *Sci. Technol. Adv. Mater.* **2001**, *2*, 147–155. [CrossRef]
114. Weidong, H.; Xingguo, G.; Yaohe, Z. Primary spacing selection of constrained dendritic growth. *J. Cryst. Growth* **1993**, *134*, 105–115. [CrossRef]
115. Ding, G.; Huang, W.; Huang, X.; Lin, X.; Zhou, Y. On primary dendritic spacing during unidirectional solidification. *Acta Mater.* **1996**, *44*, 3705–3709. [CrossRef]
116. Weidong, H. Non-steady state process and interface pattern selection of a single-phase alloy during unidirectional solidification. Ph.D. Thesis, Northwestern Polytechnical University, Xi'an, China, 1989.

117. Losert, W.; Shi, B.; Cummins, H.; Warren, J.A. Spatial period-doubling instability of dendritic arrays in directional solidification. *Phys. Rev. Lett.* **1996**, *77*, 889. [CrossRef]
118. Wan, X.; Han, Q.; Hunt, J. Different growth regimes during directional dendritic growth. *Acta Mater.* **1997**, *45*, 3975–3979. [CrossRef]
119. Esaka, H. Dendrite growth and spacing in succinonitrile-acetone alloys. Ph.D. Thesis, École Polytechnique Fédérale de Lausanne, Lausanne, Switzerland, 1986.
120. Losert, W.; Mesquita, O.; Figueiredo, J.; Cummins, H. Direct measurement of dendritic array stability. *Phys. Rev. Lett.* **1998**, *81*, 409. [CrossRef]
121. Losert, W.; Shi, B.; Cummins, H. Evolution of dendritic patterns during alloy solidification: From the initial instability to the steady state. *Proc. Natl. Acad. Sci. USA* **1998**, *95*, 439–442. [CrossRef] [PubMed]
122. Bouchard, D.; Kirkaldy, J. Scaling of intragranuiar dendritic microstructure in ingot solidification. *Metall. Mater. Trans. B* **1996**, *27*, 101–113. [CrossRef]
123. Kirkaldy, J.; Venugopalan, D. Pattern selection relations for deep-rooted binary alloy cells. *Scr. Metall.* **1989**, *23*, 1603–1608. [CrossRef]
124. Spencer, B.J.; Huppert, H.E. On the solidification of dendritic arrays: An asymptotic theory for the directional solidification of slender needle crystals. *Acta Mater.* **1997**, *45*, 1535–1549. [CrossRef]
125. Spencer, B.; Huppert, H. On the solidification of dendritic arrays: Selection of the tip characteristics of slender needle crystals by array interactions. *Acta Mater.* **1998**, *46*, 2645–2662. [CrossRef]
126. Ma, D. Modeling of primary spacing selection in dendrite arrays during directional solidification. *Metall. Mater. Trans. B* **2002**, *33*, 223–233. [CrossRef]
127. Ma, D. Response of primary dendrite spacing to varying temperature gradient during directional solidification. *Metall. Mater. Trans. B* **2004**, *35*, 735–742. [CrossRef]
128. Aveson, J.; Reinhart, G.; Goddard, C.; Nguyen-Thi, H.; Mangelinck-Noël, N.; Tandjaoui, A.; Davenport, J.; Warnken, N.; Di Gioacchino, F.; Lafford, T. On the Deformation of Dendrites During Directional Solidification of a Nickel-Based Superalloy. *Metall. Mater. Trans. A* **2019**, *50*, 5234–5241. [CrossRef]
129. Siredey, N.; Boufoussi, M.B.; Denis, S.; Lacaze, J. Dendritic growth and crystalline quality of nickel-base single grains. *J. Cryst. Growth* **1993**, *130*, 132–146. [CrossRef]
130. Husseini, N.S.; Kumah, D.P.; Jian, Z.Y.; Torbet, C.J.; Arms, D.A.; Dufresne, E.M.; Pollock, T.M.; Jones, J.W.; Clarke, R. Mapping single-crystal dendritic microstructure and defects in nickel-base superalloys with synchrotron radiation. *Acta Mater.* **2008**, *56*, 4715–4723. [CrossRef]
131. Van Hoose, J.; Grugel, R.; Tewari, S.; Brush, L.; Erdmann, R.; Poirier, D.R. Observation of Misoriented Tertiary Dendrite Arms During Controlled Directional Solidification in Aluminum-7 Wt pct Silicon Alloys. *Metall. Mater. Trans. A* **2012**, *43*, 4724–4731. [CrossRef]
132. D'Souza, N.; Newell, M.; Devendra, K.; Jennings, P.; Ardakani, M.; Shollock, B. Formation of low angle boundaries in Ni-based superalloys. *Mater. Sci. Eng. A* **2005**, *413*, 567–570. [CrossRef]
133. Newell, M.; Devendra, K.; Jennings, P.; D'Souza, N. Role of dendrite branching and growth kinetics in the formation of low angle boundaries in Ni–base superalloys. *Mater. Sci. Eng. A* **2005**, *412*, 307–315. [CrossRef]
134. Newell, M.; D'Souza, N.; Green, N. Formation of low angle boundaries in Ni-based superalloys. *Int. J. Cast Met. Res.* **2009**, *22*, 66–69. [CrossRef]
135. Aveson, J.; Tennant, P.; Foss, B.; Shollock, B.; Stone, H.; D'Souza, N. On the origin of sliver defects in single crystal investment castings. *Acta Mater.* **2013**, *61*, 5162–5171. [CrossRef]
136. Hallensleben, P.; Scholz, F.; Thome, P.; Schaar, H.; Steinbach, I.; Eggeler, G.; Frenzel, J. On crystal mosaicity in single crystal Ni-based superalloys. *Crystals* **2019**, *9*, 149. [CrossRef]
137. Bogdanowicz, W.; Krawczyk, J.; Paszkowski, R.; Sieniawski, J. Primary crystal orientation of the thin-walled area of single-crystalline turbine blade airfoils. *Materials* **2019**, *12*, 2699. [CrossRef] [PubMed]
138. Huo, M.; Liu, L.; Yang, W.; Hu, S.; Sun, D.; Su, H.; Zhang, J.; Fu, H. Dendrite growth and defects formation with increasing withdrawal rates in the rejoined platforms of Ni-based single crystal superalloys. *Vacuum* **2019**, *161*, 29–36. [CrossRef]
139. Ananth, R.; Gill, W.N. Dendritic growth in microgravity and forced convection. *J. Cryst. Growth* **1997**, *179*, 263–276. [CrossRef]

140. Das, S.K.; Gill, W.N. Foced convection heat and momentum transfer to dendritic structures (parabolic cylinders and paraboloids of revolution). *Int. J. Heat Mass Transf.* **1984**, *27*, 1345–1356.
141. KIND, M.; GILL, W.N.; ANANTH, R. The growth of ice dendrites under mixed convection conditions. *Chem. Eng. Commun.* **1987**, *55*, 295–312. [CrossRef]
142. Tirmizi, S.H.; Gill, W.N. Effect of natural convection on growth velocity and morphology of dendritic ice crystals. *J. Cryst. Growth* **1987**, *85*, 488–502. [CrossRef]
143. Ananth, R.; Gill, W.N. Dendritic growth with thermal convection. *J. Cryst. Growth* **1988**, *91*, 587–598. [CrossRef]
144. Lee, Y.-W.; Ananth, R.; Gill, W.N. Selection of a length scale in unconstrained dendritic growth with convection in the melt. *J. Cryst. Growth* **1993**, *132*, 226–230. [CrossRef]
145. Beckermann, C.; Diepers, H.-J.; Steinbach, I.; Karma, A.; Tong, X. Modeling melt convection in phase-field simulations of solidification. *J. Comput. Phys.* **1999**, *154*, 468–496. [CrossRef]
146. Lipton, J.; Glicksman, M.; Kurz, W. Dendritic growth into undercooled alloy metals. *Mater. Sci. Eng.* **1984**, *65*, 57–63. [CrossRef]
147. Trivedi, R.; Kurz, W. Theory of microstructural development during rapid solidification. In *Science and Technology of the Undercooled Melt*; Springer: Dordrecht, The Netherlands, 1986; pp. 260–267.
148. Yuan, L.; Lee, P.D.; Djambazov, G.; Pericleous, K. Numerical simulation of the effect of fluid flow on solute distribution and dendritic morphology. *Int. J. Cast Met. Res.* **2009**, *22*, 204–207. [CrossRef]
149. Yuan, L.; Lee, P.D. Dendritic solidification under natural and forced convection in binary alloys: 2D versus 3D simulation. *Modell. Simul. Mater. Sci. Eng.* **2010**, *18*, 055008. [CrossRef]
150. Zhu, M.F.; Lee, S.Y.; Hong, C.P. Modified cellular automaton model for the prediction of dendritic growth with melt convection. *PhRvE* **2004**, *69*, 061610. [CrossRef]
151. Zhu, M.-F.; Dai, T.; Lee, S.-Y.; Hong, C.-P. Modeling of solutal dendritic growth with melt convection. *Comput. Math. Appl.* **2008**, *55*, 1620–1628. [CrossRef]
152. Zhao, P.; Heinrich, J.; Poirier, D.R. Numerical modeling of fluid–particle interactions. *Comput. Methods Appl. Mech. Eng.* **2006**, *195*, 5780–5796. [CrossRef]
153. Yang, X.L.; Dong, H.B.; Wang, W.; Lee, P.D. Microscale simulation of stray grain formation in investment cast turbine blades. *Mater. Sci. Eng. A* **2004**, *386*, 129–139. [CrossRef]
154. Yang, X.; Ness, D.; Lee, P.D.; D'Souza, N. Simulation of stray grain formation during single crystal seed melt-back and initial withdrawal in the Ni-base superalloy CMSX4. *Mater. Sci. Eng. A* **2005**, *413–414*, 571–577. [CrossRef]
155. Lee, P.D.; Chirazi, A.; Atwood, R.C.; Wang, W. Multiscale modelling of solidification microstructures, including microsegregation and microporosity, in an Al–Si–Cu alloy. *Mater. Sci. Eng. A* **2004**, *365*, 57–65. [CrossRef]
156. Wang, W.; Kermanpur, A.; Lee, P.D.; McLean, M. Simulation of dendritic growth in the platform region of single crystal superalloy turbine blades. *JMatS* **2003**, *38*, 4385–4391.
157. Sun, Q.Y.; Ren, Y.; Liu, D.-R. Numerical investigations of freckles in directionally solidified nickel-based superalloy casting with abrupt contraction in cross section. *Results Phys.* **2019**, *12*, 1547–1558. [CrossRef]
158. Chen, R.; Xu, Q.; Liu, B. Cellular automaton simulation of three-dimensional dendrite growth in Al–7Si–Mg ternary aluminum alloys. *Comput. Mater. Sci.* **2015**, *105*, 90–100. [CrossRef]
159. Zhang, X.; Zhao, J. Dendritic microstructure formation in a directionally solidified Al–11.6 Cu–0.85 Mg alloy. *J. Cryst. Growth* **2014**, *391*, 52–58. [CrossRef]
160. Reuther, K.; Rettenmayr, M. Perspectives for cellular automata for the simulation of dendritic solidification–A review. *Comput. Mater. Sci.* **2014**, *95*, 213–220. [CrossRef]
161. Dong, H.; Yang, X.; Lee, P.; Wang, W. Simulation of equiaxed growth ahead of an advancing columnar front in directionally solidified Ni-based superalloys. *J. Mater. Sci.* **2004**, *39*, 7207–7212. [CrossRef]
162. Karma, A.; Rappel, W.-J. Phase-field simulation of three-dimensional dendrites: Is microscopic solvability theory correct? *J. Cryst. Growth* **1997**, *174*, 54–64. [CrossRef]
163. Takaki, T.; Shimokawabe, T.; Ohno, M.; Yamanaka, A.; Aoki, T. Unexpected selection of growing dendrites by very-large-scale phase-field simulation. *J. Cryst. Growth* **2013**, *382*, 21–25. [CrossRef]
164. Kobayashi, R.; Warren, J.; Carter, W. Mathematical models for solidification and grain boundary formation. *Achmodels Chem.* **1998**, *135*, 287–295.

165. Amoorezaei, M.; Gurevich, S.; Provatas, N. Orientation selection in solidification patterning. *Acta Mater.* **2012**, *60*, 657–663. [CrossRef]
166. Eiken, J. Dendritic growth texture evolution in Mg-based alloys investigated by phase-field simulation. *Int. J. Cast Met. Res.* **2009**, *22*, 86–89. [CrossRef]
167. Tourret, D.; Karma, A. Growth competition of columnar dendritic grains: A phase-field study. *Acta Mater.* **2015**, *82*, 64–83. [CrossRef]
168. Takaki, T.; Ohno, M.; Shimokawabe, T.; Aoki, T. Two-dimensional phase-field simulations of dendrite competitive growth during the directional solidification of a binary alloy bicrystal. *Acta Mater.* **2014**, *81*, 272–283. [CrossRef]
169. Li, J.; Wang, Z.; Wang, Y.; Wang, J. Phase-field study of competitive dendritic growth of converging grains during directional solidification. *Acta Mater.* **2012**, *60*, 1478–1493. [CrossRef]
170. Amoorezaei, M.; Gurevich, S.; Provatas, N. Spacing characterization in Al–Cu alloys directionally solidified under transient growth conditions. *Acta Mater.* **2010**, *58*, 6115–6124. [CrossRef]
171. Gurevich, S.; Karma, A.; Plapp, M.; Trivedi, R. Phase-field study of three-dimensional steady-state growth shapes in directional solidification. *Phys. Rev. E* **2010**, *81*, 011603. [CrossRef]
172. Bergeon, N.; Tourret, D.; Chen, L.; Debierre, J.-M.; Guérin, R.; Ramirez, A.; Billia, B.; Karma, A.; Trivedi, R. Spatiotemporal dynamics of oscillatory cellular patterns in three-dimensional directional solidification. *Phys. Rev. Lett.* **2013**, *110*, 226102. [CrossRef]
173. Greenwood, M.; Haataja, M.; Provatas, N. Crossover scaling of wavelength selection in directional solidification of binary alloys. *Phys. Rev. Lett.* **2004**, *93*, 246101. [CrossRef]
174. Steinbach, I. Effect of interface anisotropy on spacing selection in constrained dendrite growth. *Acta Mater.* **2008**, *56*, 4965–4971. [CrossRef]
175. Zhao, Y.; Zhang, B.; Hou, H.; Chen, W.; Wang, M. Phase-field simulation for the evolution of solid/liquid interface front in directional solidification process. *J. Mater. Sci. Technol.* **2019**, *35*, 1044–1052. [CrossRef]
176. Takaki, T.; Fukuoka, T.; Tomita, Y. Phase-field simulation during directional solidification of a binary alloy using adaptive finite element method. *J. Cryst. Growth* **2005**, *283*, 263–278. [CrossRef]
177. Gurevich, S.; Amoorezaei, M.; Montiel, D.; Provatas, N. Evolution of microstructural length scales during solidification of magnesium alloys. *Acta Mater.* **2012**, *60*, 3287–3295. [CrossRef]
178. Montiel, D.; Gurevich, S.; Ofori-Opoku, N.; Provatas, N. Characterization of late-stage equiaxed solidification of alloys. *Acta Mater.* **2014**, *77*, 183–190. [CrossRef]
179. Echebarria, B.; Karma, A.; Gurevich, S. Onset of sidebranching in directional solidification. *Phys. Rev. E* **2010**, *81*, 021608. [CrossRef]
180. Sun, Y.; Beckermann, C. Effect of solid–liquid density change on dendrite tip velocity and shape selection. *J. Cryst. Growth* **2009**, *311*, 4447–4453. [CrossRef]
181. Galenko, P.; Abramova, E.; Jou, D.; Danilov, D.; Lebedev, V.; Herlach, D.M. Solute trapping in rapid solidification of a binary dilute system: A phase-field study. *Phys. Rev. E* **2011**, *84*, 041143. [CrossRef] [PubMed]
182. Zhang, L.; Danilova, E.V.; Steinbach, I.; Medvedev, D.; Galenko, P.K. Diffuse-interface modeling of solute trapping in rapid solidification: Predictions of the hyperbolic phase-field model and parabolic model with finite interface dissipation. *Acta Mater.* **2013**, *61*, 4155–4168. [CrossRef]
183. Wang, H.; Liu, F.; Ehlen, G.; Herlach, D. Application of the maximal entropy production principle to rapid solidification: A multi-phase-field model. *Acta Mater.* **2013**, *61*, 2617–2627. [CrossRef]
184. Wang, H.; Kuang, W.; Zhang, X.; Liu, F. A hyperbolic phase-field model for rapid solidification of a binary alloy. *J. Mater. Sci.* **2015**, *50*, 1277–1286. [CrossRef]
185. Mullis, A. Prediction of the operating point of dendrites growing under coupled thermosolutal control at high growth velocity. *Phys. Rev. E* **2011**, *83*, 061601. [CrossRef] [PubMed]
186. Akamatsu, S.; Plapp, M. Eutectic and peritectic solidification patterns. *Curr. Opin. Solid State Mater. Sci.* **2016**, *20*, 46–54. [CrossRef]
187. Kobayashi, R.; Warren, J.A.; Carter, W.C. A continuum model of grain boundaries. *Phys. D Nonlinear Phenom.* **2000**, *140*, 141–150. [CrossRef]
188. Steinbach, I.; Pezzolla, F.; Nestler, B.; Seeßelberg, M.; Prieler, R.; Schmitz, G.J.; Rezende, J.L. A phase field concept for multiphase systems. *Phys. D Nonlinear Phenom.* **1996**, *94*, 135–147. [CrossRef]

189. Vanherpe, L.; Moelans, N.; Blanpain, B.; Vandewalle, S. Bounding box algorithm for three-dimensional phase-field simulations of microstructural evolution in polycrystalline materials. *Phys. Rev. E* **2007**, *76*, 056702. [CrossRef]
190. Eiken, J.; Böttger, B.; Steinbach, I. Multiphase-field approach for multicomponent alloys with extrapolation scheme for numerical application. *Phys. Rev. E* **2006**, *73*, 066122. [CrossRef]
191. Choudhury, A.; Nestler, B. Grand-potential formulation for multicomponent phase transformations combined with thin-interface asymptotics of the double-obstacle potential. *Phys. Rev. E* **2012**, *85*, 021602. [CrossRef] [PubMed]
192. Moelans, N. A quantitative and thermodynamically consistent phase-field interpolation function for multi-phase systems. *Acta Mater.* **2011**, *59*, 1077–1086. [CrossRef]
193. Ohno, M. Quantitative phase-field modeling of nonisothermal solidification in dilute multicomponent alloys with arbitrary diffusivities. *Phys. Rev. E* **2012**, *86*, 051603. [CrossRef]
194. Zhang, L.; Steinbach, I. Phase-field model with finite interface dissipation: Extension to multi-component multi-phase alloys. *Acta Mater.* **2012**, *60*, 2702–2710. [CrossRef]
195. Tiaden, J.; Nestler, B.; Diepers, H.-J.; Steinbach, I. The multiphase-field model with an integrated concept for modelling solute diffusion. *Phys. D Nonlinear Phenom.* **1998**, *115*, 73–86. [CrossRef]
196. Bottger, B.; Eiken, J.; Steinbach, I. Multi phase-field approach for alloy solidification. *Phys Rev E* **2006**, *73*, 066122–1.
197. Steinbach, I.; Pezzolla, F. A generalized field method for multiphase transformations using interface fields. *Phys. D Nonlinear Phenom.* **1999**, *134*, 385–393. [CrossRef]
198. Steinbach, I.; Apel, M. Multi phase field model for solid state transformation with elastic strain. *Phys. D Nonlinear Phenom.* **2006**, *217*, 153–160. [CrossRef]
199. Kim, S.G. A phase-field model with antitrapping current for multicomponent alloys with arbitrary thermodynamic properties. *Acta Mater.* **2007**, *55*, 4391–4399. [CrossRef]
200. Ofori-Opoku, N.; Provatas, N. A quantitative multi-phase field model of polycrystalline alloy solidification. *Acta Mater.* **2010**, *58*, 2155–2164. [CrossRef]
201. Yamanaka, A.; Aoki, T.; Ogawa, S.; Takaki, T. GPU-accelerated phase-field simulation of dendritic solidification in a binary alloy. *J. Cryst. Growth* **2011**, *318*, 40–45. [CrossRef]
202. Shimokawabe, T.; Aoki, T.; Takaki, T.; Endo, T.; Yamanaka, A.; Maruyama, N.; Nukada, A.; Matsuoka, S. Peta-Scale Phase-Field Simulation for Dendritic Solidification on the TSUBAME 2.0 Supercomputer. In Proceedings of the 2011 International Conference for High Performance Computing, Networking, Storage and Analysis, Seattle, WA, USA, 12–18 November 2011; ACM: New York, NY, USA, 2011; p. 3.
203. Takaki, T.; Sakane, S.; Ohno, M.; Shibuta, Y.; Shimokawabe, T.; Aoki, T. Primary arm array during directional solidification of a single-crystal binary alloy: Large-scale phase-field study. *Acta Mater.* **2016**, *118*, 230–243. [CrossRef]
204. Takaki, T. Phase-field modeling and simulations of dendrite growth. *ISIJ Int.* **2014**, *54*, 437–444. [CrossRef]
205. Kobayashi, R. Modeling and numerical simulations of dendritic crystal growth. *Phys. D Nonlinear Phenom.* **1993**, *63*, 410–423. [CrossRef]
206. Bergeon, N.; Ramirez, A.; Chen, L.; Billia, B.; Gu, J.; Trivedi, R. Dynamics of interface pattern formation in 3D alloy solidification: First results from experiments in the DECLIC directional solidification insert on the International Space Station. *J. Mater. Sci.* **2011**, *46*, 6191–6202. [CrossRef]
207. Tourret, D.; Debierre, J.-M.; Song, Y.; Mota, F.L.; Bergeon, N.; Guerin, R.; Trivedi, R.; Billia, B.; Karma, A. Oscillatory cellular patterns in three-dimensional directional solidification. *Phys. Rev. E* **2015**, *92*, 042401. [CrossRef]
208. Bergeon, N.; Trivedi, R.; Billia, B.; Echebarria, B.; Karma, A.; Liu, S.; Weiss, C.; Mangelinck, N. Necessity of investigating microstructure formation during directional solidification of transparent alloys in 3D. *Adv. Space Res.* **2005**, *36*, 80–85. [CrossRef]
209. Ramirez, A.; Chen, L.; Bergeon, N.; Billia, B.; Gu, J.; Trivedi, R. *In Situ and Real Time Characterization of Interface Microstructure in 3D Alloy Solidification: BENCHMARK Microgravity Experiments in the DECLIC-Directional Solidification Insert on ISS*; IOP Conference Series: Materials Science and Engineering; IOP Publishing: Bristol, UK, 2012; p. 012087.
210. Sturz, L.; Zimmermann, G.; Rex, S.; Mathes, M.; Kauerauf, B. Analysis of diffusive cellular patterns in directional solidification of bulk samples. *Metall. Mater. Trans. A* **2004**, *35*, 239–246. [CrossRef]

211. Rex, S.; Kauerauf, B.; Zimmermann, G. Directional solidification of cellular arrays in a transparent organic alloy. *Adv. Space Res.* **2002**, *29*, 511–520. [CrossRef]
212. Wang, Y.; Jia, S.; Wei, M.; Peng, L.; Wu, Y.; Ji, Y.; Chen, L.-Q.; Liu, X. Coupling in situ synchrotron X-ray radiography and phase-field simulation to study the effect of low cooling rates on dendrite morphology during directional solidification in Mg–Gd alloys. *J. Alloy. Compd.* **2020**, *815*, 152385. [CrossRef]
213. Yang, M.; Xiong, S.; Guo, Z. Dendrite Morphology and Growth Orientation of Magnesium Alloys: Simulation by Phase-Field and 3-D Characterization by Synchrotron X-Ray Tomography. In *Magnesium Technology 2016*; Springer: Cham, Switzerland, 2016; pp. 35–39.
214. Chen, Y.; Li, D.Z.; Billia, B.; Nguyen-Thi, H.; Qi, X.B.; Xiao, N.M. Quantitative phase-field simulation of dendritic equiaxed growth and comparison with in situ observation on Al–4 wt.% Cu alloy by means of synchrotron X-ray radiography. *ISIJ Int.* **2014**, *54*, 445–451. [CrossRef]
215. Mathiesen, R.H.; Arnberg, L.; Mo, F.; Weitkamp, T.; Snigirev, A. Time resolved x-ray imaging of dendritic growth in binary alloys. *Phys. Rev. Lett.* **1999**, *83*, 5062. [CrossRef]
216. Mathiesen, R.; Arnberg, L.; Nguyen-Thi, H.; Billia, B. In situ x-ray video microscopy as a tool in solidification science. *JOM* **2012**, *64*, 76–82. [CrossRef]
217. Shuai, S.; Guo, E.; Phillion, A.; Callaghan, M.D.; Jing, T.; Lee, P.D. Fast synchrotron X-ray tomographic quantification of dendrite evolution during the solidification of MgSn alloys. *Acta Mater.* **2016**, *118*, 260–269. [CrossRef]
218. Cai, B.; Wang, J.; Kao, A.; Pericleous, K.; Phillion, A.; Atwood, R.; Lee, P. 4D synchrotron X-ray tomographic quantification of the transition from cellular to dendrite growth during directional solidification. *Acta Mater.* **2016**, *117*, 160–169. [CrossRef]
219. Cai, B.; Karagadde, S.; Yuan, L.; Marrow, T.; Connolley, T.; Lee, P. In situ synchrotron tomographic quantification of granular and intragranular deformation during semi-solid compression of an equiaxed dendritic Al–Cu alloy. *Acta Mater.* **2014**, *76*, 371–380. [CrossRef]
220. Bogno, A.; Nguyen-Thi, H.; Reinhart, G.; Billia, B.; Baruchel, J. Growth and interaction of dendritic equiaxed grains: In situ characterization by synchrotron X-ray radiography. *Acta Mater.* **2013**, *61*, 1303–1315. [CrossRef]
221. Azeem, M.; Lee, P.; Phillion, A.; Karagadde, S.; Rockett, P.; Atwood, R.; Courtois, L.; Rahman, K.; Dye, D. Revealing dendritic pattern formation in Ni, Fe and Co alloys using synchrotron tomography. *Acta Mater.* **2017**, *128*, 241–248. [CrossRef]
222. Winick, H. Fourth generation light sources. In Proceedings of the 1997 Particle Accelerator Conference (Cat. No. 97CH36167), Vancouver, BC, Canada, 12–16 May 1997; IEEE: New York, NY, USA, 1997; pp. 37–41.
223. Eriksson, M.; van der Veen, J.F.; Quitmann, C. Diffraction-limited storage rings–a window to the science of tomorrow. *J. Synchrotron Radiat.* **2014**, *21*, 837–842. [CrossRef]
224. Cereser, A.; Strobl, M.; Hall, S.A.; Steuwer, A.; Kiyanagi, R.; Tremsin, A.S.; Knudsen, E.B.; Shinohara, T.; Willendrup, P.K.; da Silva Fanta, A.B. Time-of-flight three dimensional neutron diffraction in transmission mode for mapping crystal grain structures. *Sci. Rep.* **2017**, *7*, 9561. [CrossRef] [PubMed]
225. Kardjilov, N.; Manke, I.; Hilger, A.; Strobl, M.; Banhart, J. Neutron imaging in materials science. *Mater. Today* **2011**, *14*, 248–256. [CrossRef]
226. Frei, G.; Lehmann, E.; Mannes, D.; Boillat, P. The neutron micro-tomography setup at PSI and its use for research purposes and engineering applications. *Nucl. Instrum. Methods Phys. Res. Sect. A Accel. Spectrometers Detect. Assoc. Equip.* **2009**, *605*, 111–114. [CrossRef]
227. Tremsin, A.; McPhate, J.; Vallerga, J.; Siegmund, O.; Hull, J.; Feller, W.; Lehmann, E. Detection efficiency, spatial and timing resolution of thermal and cold neutron counting MCP detectors. *Nucl. Instrum. Methods Phys. Res. Sect. A Accel. Spectrometers Detect. Assoc. Equip.* **2009**, *604*, 140–143. [CrossRef]
228. Tremsin, A.; McPhate, J.; Vallerga, J.; Siegmund, O.; Hull, J.; Feller, W.; Lehmann, E. High-resolution neutron radiography with microchannel plates: Proof-of-principle experiments at PSI. *Nucl. Instrum. Methods Phys. Res. Sect. A Accel. Spectrometers Detect. Assoc. Equip.* **2009**, *605*, 103–106. [CrossRef]
229. Peetermans, S.; Lehmann, E. Simultaneous neutron transmission and diffraction contrast tomography as a non-destructive 3D method for bulk single crystal quality investigations. *J. Appl. Phys.* **2013**, *114*, 124905. [CrossRef]
230. Peetermans, S.; King, A.; Ludwig, W.; Reischig, P.; Lehmann, E. Cold neutron diffraction contrast tomography of polycrystalline material. *Analyst* **2014**, *139*, 5765–5771. [CrossRef]

231. Nenchev, B.; Strickland, J.; Tassenberg, K.; Perry, S.; Gill, S.; Dong, H. Automatic Recognition of Dendritic Solidification Structures: DenMap. *J. Imaging* **2020**, *6*, 19. [CrossRef]
232. Strickland, J.; Nenchev, B.; Dong, H. *Applications of Pattern Recognition for Dendritic Microstructures*; IOP Conference Series: Materials Science and Engineering; IOP Publishing: Bristol, UK, 2020; p. 012057.